The solid effect of dynamic nuclear polarization in liquids II: Accounting for g-tensor anisotropy at high magnetic fields

Deniz Sezer, Danhua Dai, and Thomas F. Prisner

Institute of Physical and Theoretical Chemistry, Goethe University, 60438 Frankfurt am Main, Germany

Correspondence: Deniz Sezer (dzsezer@gmail.com)

Abstract. In spite of its name, the solid effect of dynamic nuclear polarization (DNP) is operative also in viscous liquids, where the dipolar interaction between the polarized nuclear spins and the polarizing electrons is not completely averaged out by molecular diffusion. Under such slow-motional conditions, it is likely that the tumbling of the polarizing agent is similarly too slow to efficiently average the anisotropies of its magnetic tensors. Here we extend our previous analysis of the solid effect in

5   liquids to account for the effect of g-tensor anisotropy at high magnetic fields. Building directly on the mathematical treatment of slow-tumbling in electron spin resonance (Freed et al., 1971), we calculate solid-effect DNP enhancements in the presence of both translational diffusion of the liquid molecules and rotational diffusion of the polarizing agent. To illustrate the formalism, we analyze high-field (9.4 T) DNP enhancement profiles from nitroxide-labeled lipids in fluid lipid bilayers. By properly accounting for power-broadening and motional-broadening, we successfully decompose the measured DNP enhancements

10   into their separate contributions from the solid and Overhauser effects.

1 Introduction

The sensitivity of NMR experiments is greatly increased by dynamic nuclear polarization (DNP),[1] where the much larger static polarization that is available to electronic spins is transferred to nuclear spins (Wenckebach, 2016). For the transfer to take place, the electronic and nuclear spins should be able to flip simultaneously (Abragam and Goldman, 1978). Such concerted

15   flips correspond to the zero-quantum (ZQ) and double-quantum (DQ) transitions of the electron-nucleus spin system, which are enabled by the inter-spin interactions. Among the four DNP mechanisms, namely the Overhauser effect (OE), the solid effect (SE), the cross effect, and thermal mixing, only the first two are operative in the liquid state, where the spin-spin interactions change randomly in time due to the thermal motions of the molecules.

     In OE-DNP, the ZQ and DQ transitions are in fact possible because the dipole-dipole and contact interactions are modulated

20   by the molecular motions. In SE-DNP, on the other hand, the ZQ and DQ transitions are driven directly by the microwave (mw) excitation, and the modulation of the dipolar interaction is detrimental because it constantly modifies the matching condition that the mw frequency should satisfy in order to resonantly drive these transitions.

---

[1] Abbreviations used in the text: continuous wave (cw), 1,2-dioleoyl-sn-glycero-3-phosphocholine (DOPC), double quantum (DQ), dynamic nuclear polarization (DNP), electron paramagnetic resonance (EPR), force-free hard sphere (FFHS), microwave (mw), nuclear magnetic resonance (NMR), Overhauser effect (OE), 1-palmitoyl-2-stearoyl-sn-glycero-3-phosphocholine (PSPC), solid effect (SE), stochastic Liouville equation (SLE), zero quantum (ZQ).

The initial theoretical treatments of OE (Solomon, 1955) and SE (Abragam and Proctor, 1958) modeled the ZQ and DQ transitions by expressing the transition probabilities per unit time using Fermi's golden rule. As the mathematical description

25 of (semi-classical) relaxation theory matured around the same time (Redfield, 1957; Abragam, 1961), the Fermi golden rule was promptly replaced in the theory of OE-DNP in liquids (Hausser et al., 1968) by the correlation function of the dipolar interaction (or its Laplace transform, which is known as spectral density). Because the time-domain description of relaxation leads to a correlation function in a very general way (Abragam, 1961), the same formalism works naturally with different spectral densities (e.g., for rotational or translational diffusion). As an example, the improved analytical treatment of translational

30 diffusion achieved in 1975 was immediately applied to paramagnetic relaxation in liquids (Ayant et al., 1975; Hwang and Freed, 1975).[2]

During the same time period, it also became possible to account for spin dephasing and relaxation beyond second order (Anderson, 1954; Kubo, 1954), which is important for understanding spectral line shapes outside the regime of fast averaging (Kubo, 1969). These initial ideas were transformed into a powerful tool for the calculation and analysis of slow-motional EPR

35 spectra by Freed et al. (1971).

When first presented, Abragam's quantitative description of SE-DNP in terms of mixing of the Zeeman energy levels by the dipolar interaction (Abragam and Proctor, 1958) conclusively explained that the NMR signal is maximally enhanced when the mw frequency is shifted from the electronic resonance by $\pm\omega_I$, where ω_I is the Larmor frequency of the polarized nuclear spin. Abragam's perturbative analysis also correctly predicted that the effect should drop quadratically with the magnitude of the

40 static magnetic field, which has lasting implications for SE-DNP at high magnetic fields. In spite of these successes, however, the perturbative approach to SE is practically impossible to integrate with other relevant spin phenomena whose mathematical treatment matured subsequently.

Recently, Sezer (2023a) presented a time-domain description of SE which, like semi-classical relaxation theory, allows for different dynamical processes to modulate the relevant spin interactions. By interfacing this description with the spectral

45 density of translational diffusion (Ayant et al., 1975; Hwang and Freed, 1975), it was possible to treat SE-DNP in the presence of molecular translation (Sezer, 2023b), as relevant to liquids. The requirement that the dipolar interaction should not be completely averaged out by the molecular dynamics restricts liquid-state SE-DNP to viscous media, where the tumbling of the polarizing agent may similarly be too slow to average the anisotropies of its magnetic tensors. The current paper accounts for the effect of g-tensor anisotropy on SE in this slow-tumbling regime. To this end, the time-domain description of SE-DNP in

50 liquids is interfaced here with the established mathematical treatment of slow-motional EPR spectra (Freed et al., 1971).

To motivate the presented theoretical study, in Sec. 2 we formulate one specific practical problem that it addresses. There we also introduce the experimental EPR and DNP data that are analyzed subsequently in Sec. 5 using the developed theory. The needed background from Sezer (2023a, b) is presented in Sec. 3. Building on it, in Sec. 4 we adapt the slow-motional formalism of Freed et al. (1971) to the treatment of SE in the liquid state. Our conclusions are in Sec. 6, and several supporting

55 figures are left to the appendix.

---

[2]Surprisingly, this improved treatment is not mentioned by Müller-Warmuth et al. (1983), who continue to use the older, deficient expression of the spectral density for translational diffusion.

2 Motivation

DNP aims to increase the longitudinal nuclear magnetization, i_z, beyond its equilibrium Boltzmann value, i_z^{eq}. This is done by doping the sample with unpaired electrons, whose spins are then subjected to near-resonance microwave irradiation. In continuous-wave (cw) DNP, which is the only variety that we consider here, a steady state magnetization i_z^{ss} is reached after the microwaves have been applied for sufficiently long time. The enhancement of i_z under such steady-state conditions is

$$\epsilon = \frac{i_z^{\text{ss}}}{i_z^{\text{eq}}} - 1, \tag{1}$$

where $\epsilon = 0$ corresponds to the absence of DNP.

In both OE and SE, ϵ is directly proportional to the ratio of the gyromagnetic factors of the electronic and nuclear spins, γ_S and γ_I. For OE (Hausser et al., 1968; Müller-Warmuth et al., 1983),

$$\epsilon_{\text{OE}} = scf \frac{|\gamma_S|}{\gamma_I}, \tag{2}$$

where s, c and f are, respectively, the electronic saturation factor, the coupling factor and the leakage factor. The former is defined as

$$s = 1 - s_z^{\text{ss}}/s_z^{\text{eq}} \tag{3}$$

and reflects the deviation of the longitudinal electronic magnetization at steady state, s_z^{ss}, from its equilibrium value, s_z^{eq}. The other two factors, c and f, quantify the interaction between the electronic and nuclear spins. Specifically,

$$f = 1 - T_{1I}/T_{1I}^0 \tag{4}$$

compares the nuclear T_1's in the presence (T_{1I}) and in the absence (T_{1I}^0) of the polarizing agent. In DNP, the former is typically (much) shorter than the latter due to the elevated concentration of the electronic spins, hence $f \approx 1$.

Similarly, the SE enhancement can be expressed as (Sezer, 2023a)

$$\epsilon_{\text{SE}} = p v_- T_{1I} \left(\frac{1}{1 + v_+ T_{1I}} \right) \frac{|\gamma_S|}{\gamma_I}, \tag{5}$$

where $p = 1 - s$ quantifies how "non-saturated" the electronic transition is, and the rate constants $v_\pm$ are related to the ability of the microwaves to excite simultaneous flips of the electronic and nuclear spins. These concerted flips correspond to the "forbidden" ZQ and DQ transitions, which are enabled by the dipolar interaction. In fact,

$$v_\pm = v_2 \pm v_0, \tag{6}$$

where v_0 and v_2 denote, respectively, the ZQ and DQ transition rates. In liquids, where the dipolar interaction is partially averaged, the contribution of the mw excitation to the nuclear relaxation rate $R_{1I} = 1/T_{1I}$, which is quantified by v_+, is generally negligibly small. As a result, $v_+/R_{1I} \ll 1$ and the expression in parenthesis in (5) is essentially one. Then the SE enhancement acquires the multiplicative form

$$\epsilon_{\text{SE}} \approx p v_- T_{1I} \frac{|\gamma_S|}{\gamma_I} \qquad (v_+ \ll R_{1I}), \tag{7}$$

85   which is analogous to ϵ_{OE} with the factors s, c and f being replaced by the factors p, v_- and T_{1I}, respectively. In the numerical work presented in Sec. 5 we use the approximation (7). The condition $v_+ T_{1I} \ll 1$ is validated at the end of the analysis by comparing the estimated v_+ to the measured T_{1I}.

   In the current paper we study the dependence of the DNP enhancement on the displacement from the electronic resonance. Following Gizatullin et al. (2022), we call the profile of ϵ against the offset from resonance a "DNP spectrum". Because DNP

90 experiments in the liquid state are carried out with a mw resonator (Erb et al., 1958a, b; Leblond et al., 1971b; Neudert et al., 2016; Gizatullin et al., 2021a; Kuzhelev et al., 2022, 2023), off-resonance conditions are achieved by varying the stationary magnetic field at constant mw frequency (i.e., field sweep). In theoretical analysis, however, it is more convenient to work with a fixed B_0 and a variable mw frequency. Thus, when comparing calculations and experiments, we will convert the horizontal axis of the experiments from magnetic field to offset frequency.

95   In the case of ϵ_{OE} (eq. (2)), the entire offset dependence is due to the saturation factor s, as the factors c and f are practically constant over such narrow frequency range. In the case of ϵ_{SE} (eq. (5)), both pv_- and v_+ are functions of the offset. For a single, homogeneously-broadened EPR line the saturation factor can be obtained in closed analytical form from the Bloch equations (as we review below in Sec. 3.1). Recently Sezer (2023a) showed that the SE spin dynamics is described by two coupled Bloch equations, whose steady state can similarly be solved analytically to obtain closed-form expressions for the rate

100 constants $v_\pm$ (reviewed in Sec. 3.2). In liquids, where the random molecular motion modulates the dipolar interaction between the electronic and nuclear spins, these rate constants are no longer available analytically but can be calculated numerically for motional models with known dipolar spectral densities (Sezer, 2023b), as reviewed below in Sec. 3.3.

   Liquid-state SE-DNP is restricted to viscous media, where the dipolar interaction is not averaged out completely by the molecular motions. Under these conditions, the tumbling of the polarizing agent is also expected to be too slow to average the

105 anisotropies of its magnetic tensors. One thus expects substantial deviations from the Lorentzian EPR line shape of the Bloch equations. Such deviations are unavoidable in the case of nitroxide-based polarizing agents whose g and A tensors are rather anisotropic. A recent SE-DNP study at 9.4 T demonstrated that even the narrow-line radical trityl exhibited g-tensor broadening in liquid glycerol (Kuzhelev et al., 2023).

   This paper extends the theoretical description of SE-DNP to the regime of slow radical tumbling where the cw-EPR spectrum

110 deviates from a Lorentzian line. Given our longstanding efforts in liquid-state DNP at 9.4 T, here we focus on high magnetic fields, where the width of the EPR spectrum is dominated by the anisotropy of the g tensor. We will thus completely neglect the hyperfine tensor. This possibility will greatly simplify the needed adjustments to the Lorentzian case (Sec. 4).

   To illustrate the practical problem that motivated this theoretical work, we now turn to the experimental data in fig. 1. The characterized samples comprised liposomes of hydrated lipid bilayers composed of DOPC (1,2-dioleoyl-sn-glycero-3-

115 phosphocholine) lipids. As the phase transition temperature of DOPC is about $-17\,^{\circ}\mathrm{C}$, the lipids were in their fluid, liquid-crystalline phase in the experiments at $\approx 320\,\mathrm{K}$. The DOPC lipids were mixed at a ratio of 20:1 with PSPC lipids spin-labeled either at position 10 (1-palmitoyl-2-stearoyl-(10-doxyl)-sn-glycero-3-phosphocholine) or at position 16 along one of their aliphatic chains. Both the EPR spectra (fig. 1a,b) and the DNP enhancements (fig. 1c,d) were recorded in our home-built Fabry-Pérot resonator at 9.4 T, equipped with temperature control (Denysenkov et al., 2022). While the target temperature of
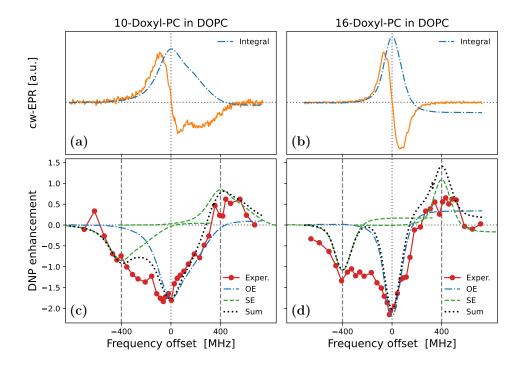
Figure 1. Experimental cw-EPR spectra (**a**, **b**) and DNP spectra (**c**, **d**) of spin-labeled lipids in DOPC lipid bilayers at 9.4 T and ≈ 320 K. The nitroxide spin label (Doxyl) is either at position 10 (**a**, **c**) or at position 16 (**b**, **d**) of the aliphatic lipid chain. The integrated cw-EPR spectra (dashed-dotted blue lines in **a** and **b**) are used to decompose the DNP spectra (**c** and **d**) into contributions from OE (dashed-dotted blue lines) and SE (dashed green lines).

120 the experiments was 320 K, an extra temperature rise of less than $10\,^{\circ}$C can be expected at the maximum mw power of 5.5 W that was used for DNP (Denysenkov et al., 2022). Details about the experiments and the sample preparation will be published elsewhere.

The cw-EPR spectrum of 10-Doxyl-PC in fig. 1a (orange line) is seen to deviate substantially from (the derivative of) a Lorentzian line shape. At this high magnetic field, the EPR line width is expected to be dominated by the large anisotropy of

125 the nitroxide g tensor, with comparatively much smaller contribution from the nitroxide hyperfine tensor. (These expectations are tested and verified below in Sec. 5.1.) For comparison, in fig. 1b we show the cw-EPR spectrum of the sample doped with 16-Doxyl-PC. Visually, this narrower spectrum more closely resembles a homogeneous Lorentzian line, although it still deviates from it (as discussed in Sec. 5.2).

In fig. 1c we show the DNP spectrum (filled red circles) of the sample containing 10-Doxyl-PC as a polarizing agent. The

130 enhanced NMR signal belongs to the acyl chain protons of the lipids. Thanks to the high magnetic field of the experiment, it was possible to resolve the NMR signal of these non-polar protons from the polar protons of water and of the lipid head groups. The DNP spectrum is seen to have a complex line shape, with the positive enhancement values at offsets of about $+400$ MHz demonstrating contribution from SE. At the same time, the comparatively larger negative enhancements in the vicinity of the

electronic resonance (i.e., around 0 MHz) point to a contribution from OE. Such coexistence of SE and OE is well documented

135 for nitroxide free radicals at the classical EPR fields of about 0.35 T (Leblond et al., 1971b; Neudert et al., 2017; Gizatullin et al., 2021a, b). Evidently, it also persists at 9.4 T. The DNP spectrum of 16-Doxyl-PC in fig. 1d also exhibits a mixture of SE and OE.

More than half a century ago Korringa and coworkers developed a rigorous theoretical framework to predict such mixed DNP spectra in viscous liquids (Papon et al., 1968; Leblond et al., 1971a). Likely because of its complexity, as well as its

140 neglect of translational diffusion, their formal analysis has not been applied to recent DNP data. As a simple and practical alternative, Neudert et al. (2017) disentangle the OE and SE components of such mixed DNP spectra using only the integral of the measured cw-EPR signal. Their approach is based on the following insightful observations: (i) up to an overall scaling factor the EPR line shape is equal to the saturation factor and thus to the OE enhancement (eq. (2)); (ii) up to an overall scaling factor the SE enhancement lines at $\pm\omega_I$ are shifted versions (and flipped for the ZQ transition) of the same EPR line shape.

145 One can thus identify the contributions of OE and SE to the DNP spectrum by placing the integrated cw-EPR spectrum at, respectively, zero and $\pm\omega_I$ offsets, and independently adjusting the magnitudes of the two components.

This approach is illustrated in figs. 1c and 1d, where the dashed-dotted blue lines are the integrals of the cw-EPR spectra from figs. 1a and 1b, respectively (flipped here to reflect the dipolar nature of OE), and the dashed green lines are the same EPR spectra but centered at -400 MHz and $+400$ MHz. The sum of the OE and SE contributions determined in this way is shown

150 with a dotted black line. This sum is seen to agree closely with the DNP spectrum of 10-Doxyl-PC (fig. 1c) and to capture well the overall shape of the DNP spectrum of 16-Doxyl-PC (fig. 1d).

In spite of the good general agreement between the experimental DNP spectra and the dotted black lines in figs. 1c and 1d, some persistent differences remain. In particular, (i) the OE feature in the experiment appears to be consistently broader than the EPR line and (ii) the enhancement between the central OE feature and the negative SE feature is consistently larger than

155 what is predicted by the overlap of the two copies of the EPR line shape. Both of these aspects are especially clear in the case of 16-Doxyl-PC (fig. 1d)

The first deficiency is easy to rationalize. Cw-EPR spectra are recorded at low mw power and their widths reflect mechanisms contributing to the electronic T_2 relaxation. The DNP spectrum, on the other hand, is recorded at high mw power, where the EPR line width experiences power-broadening that also depends on the electronic T_1 relaxation. That the OE-DNP spectrum

160 "represents an indirect observation of the electron resonance when greatly saturated" was understood early on (Carver and Slichter, 1956, fig. 6). To properly model the contribution of OE to mixed DNP spectra, therefore, it is necessary to calculate the cw-EPR spectrum under saturating conditions. How to rigorously do that in the regime of slow radical tumbling is known (Freed et al., 1971).

While power-broadening affects OE, it is not immediately clear whether one should also take it into account when modeling

165 SE. (We address this point in Sec. 4.4.) Even leaving power-broadening aside, however, we know that in liquids the SE lines of the DNP spectrum should also be broader than the EPR line width because of the fluctuations of the dipolar interaction (Sezer, 2023b). Although Sezer (2023b) showed how to quantify this additional motional broadening in the case of translational molecular diffusion, the theoretical treatment there assumed a Lorentzian EPR line and is thus not directly applicable to the

MAGNETIC
RESONANCE
Discussions

experiments in fig. 1. In the current paper, we extend the formalism to slow radical tumbling and g-tensor anisotropy (Sec. 4). In Sec. 5 we apply the developed theory to the analysis of the experimental spectra in fig. 1. The needed theoretical background is reviewed next.

3 Theoretical background

3.1 Bloch equations

The evolution of the expectation values of the electronic spin operators S_i ($i = x, y, z$), which we denote by s_i, is described by the classical Bloch equations (in the rotating frame)

$$
\begin{bmatrix} \dot{s}_x(t) \\ \dot{s}_y(t) \\ \dot{s}_z(t) \end{bmatrix} = - \begin{bmatrix} R_2 & \Delta & 0 \\ -\Delta & R_2 & \omega_1 \\ 0 & -\omega_1 & R_1 \end{bmatrix} \begin{bmatrix} s_x(t) \\ s_y(t) \\ s_z(t) \end{bmatrix} + R_1 \begin{bmatrix} 0 \\ 0 \\ s_z^{\mathrm{eq}} \end{bmatrix}.
\tag{8}
$$

Here, the dot above the variable indicates differentiation with respect to time, R_2 and R_1 are the reciprocals of the electronic relaxation times T_2 and T_1, respectively, and[3]

$$
\Delta = \omega_0 - \omega
\tag{9}
$$

is the offset between the Larmor frequency of the electronic spins, ω_0, and the (angular) frequency of the oscillating magnetic field, ω. In the case of an isotropic g-factor, g_0,

$$
\omega_0 = g_0 \mu_{\mathrm{B}} B_0 / \hbar,
\tag{10}
$$

where μ_{B} is the Bohr magneton.

At steady state

$$
\begin{bmatrix} R_2 & \Delta & 0 \\ -\Delta & R_2 & \omega_1 \\ 0 & -\omega_1 & R_1 \end{bmatrix} \begin{bmatrix} s_x^{\mathrm{ss}} \\ s_y^{\mathrm{ss}} \\ s_z^{\mathrm{ss}} \end{bmatrix} = R_1 \begin{bmatrix} 0 \\ 0 \\ s_z^{\mathrm{eq}} \end{bmatrix}.
\tag{11}
$$

Solving these algebraic equations for the variables s_i^{ss}, one can calculate the cw-EPR spectrum and the electronic saturation profile. Making use of the zeros in the first and last rows of the Bloch matrix in (11), we first express s_x^{ss} and s_z^{ss} in terms of s_y^{ss}:

$$
s_x^{\mathrm{ss}} = -\Delta T_2 s_y^{\mathrm{ss}}, \qquad s_z^{\mathrm{ss}} = \omega_1 T_1 s_y^{\mathrm{ss}} + s_z^{\mathrm{eq}}.
\tag{12}
$$

The middle row of the matrix then yields

$$
s_y^{\mathrm{ss}} = -\omega_1 P_0^{-1} s_z^{\mathrm{eq}},
\tag{13}
$$

---

[3]In Sezer (2023a, b) the frequency offset was denoted by Ω. Here we reserve this symbol for the orientation of the polarizing agent (Sec. 4).

where we defined

$$P_0 = R_2 + \omega_1^2 T_1 + \Delta^2 T_2. \tag{14}$$

The in-phase (absorptive) and the out-of-phase (dispersive) components of the cw-EPR signal are then found to be

$$\mathrm{abs} = s_y^{\mathrm{ss}}/s_z^{\mathrm{eq}} = -\omega_1 P_0^{-1}$$

195 $$\mathrm{dsp} = s_x^{\mathrm{ss}}/s_z^{\mathrm{eq}} = -\Delta T_2 \, \mathrm{abs}. \tag{15}$$

From the longitudinal component at steady state we similarly find

$$s = 1 - s_z^{\mathrm{ss}}/s_z^{\mathrm{eq}} = -\omega_1 T_1 \, \mathrm{abs}, \tag{16}$$

which shows that the saturation factor is directly proportional to the absorptive EPR line shape. This proportionality holds for all mw powers, including the large powers used in DNP. In Sec. 4.3 we show that it remains valid also in the case of g-tensor

200 anisotropy.

When generalizing the Bloch equations to non-isotropic g tensor, we will need to work with high-dimensional abstract vectors. To distinguish these vectors from the vectors in 3D space, we will denote the latter by placing an arrow above their symbols, and will use bold symbols for the former. (A 3D unit vector will be indicated with a hat rather than an arrow.) Additionally, we will use capital hollow letters to denote 3×3 matrices that act on the 3D vectors. With this understanding, we

205 will write the Bloch equations (8) as

$$\dot{\vec{s}}(t) = -\mathbb{B}_0 \vec{s}(t) + R_1 \hat{k} s_z^{\mathrm{eq}}, \tag{17}$$

where

$$\vec{s}(t) = \begin{bmatrix} s_x(t) \\ s_y(t) \\ s_z(t) \end{bmatrix}, \qquad \hat{k} = \begin{bmatrix} 0 \\ 0 \\ 1 \end{bmatrix}, \tag{18}$$

210 $$\mathbb{B} = \begin{bmatrix} R_2 + \mathrm{i}\omega_I & \Delta & 0 \\ -\Delta & R_2 + \mathrm{i}\omega_I & \omega_1 \\ 0 & -\omega_1 & R_1 + \mathrm{i}\omega_I \end{bmatrix}, \tag{19}$$

and $\mathbb{B}_0 = \mathbb{B}(\omega_I = 0)$. (The subscript of $\mathbb{B}_0$ is a reminder that $\mathbb{B}$ is evaluated at $\omega_I = 0$, where ω_I is the Larmor frequency of the polarized nuclear spin.)

3.2 Solid effect in solids

SE relies on the dipolar interaction between the electronic and nuclear spins whose coupling is

215 $$A_1 = D_{\mathrm{dip}} \frac{-3\cos\theta\sin\theta}{r^3} e^{\mathrm{i}\phi}. \tag{20}$$

Here $D_{\mathrm{dip}} = (\mu_0/4\pi)\hbar\gamma_S\gamma_I$ is the dipolar constant, which equals approximately $2\pi(79\,\mathrm{kHz}\,\mathrm{nm}^3)$ for protons, and (r,θ,ϕ) are the spherical polar coordinates of the inter-spin vector.

In liquids, A_1 changes in time because of molecular diffusion. The treatment of SE-DNP for time-dependent A_1 in Sezer (2023b) was developed under the assumption that the nuclear T_1 is orders of magnitude larger than the correlation time of the dipolar interaction, which is practically always the case in liquids. For the same analysis to apply to solids, spin diffusion should be much faster than the nuclear T_1, which is not necessarily true in practice. When accounting for g-tensor anisotropy below, we will similarly assume that the tumbling of the radical is much faster than the nuclear T_1. This assumption is clearly violated in solids where "tumbling" is infinitely slow. Nevertheless, for the purposes of comparison, we will refer in the following to 'solids' with the understanding that the correlation time of the dipolar interaction is infinitely long (but still much shorter than the nuclear T_1). Because we will keep all other parameters, including the time scale of radical tumbling, the same when comparing 'solids' and liquids, it should be kept in mind that our treatment is not a good model for the solid state (hence the quotation marks).

For SE-DNP, in addition to the Bloch equations it is necessary to consider the following dynamical equations of the electron-nucleus coherences $g_i = \langle S_i I_+ \rangle$ $(i = x, y, z)$ (Sezer, 2023a):

$$
\begin{bmatrix} \dot{g}_x(t) \\ \dot{g}_y(t) \\ \dot{g}_z(t) \end{bmatrix} = -\mathbb{B} \begin{bmatrix} g_x(t) \\ g_y(t) \\ g_z(t) \end{bmatrix} - \frac{1}{4}A_1 \begin{bmatrix} s_y(t) \\ -s_x(t) \\ 0 \end{bmatrix} - \mathrm{i}\frac{1}{4}A_1 \begin{bmatrix} 0 \\ 0 \\ i_z(t) \end{bmatrix}. \tag{21}
$$

Again, we are only interested in the steady state of the dynamics where

$$
\mathbb{B} \begin{bmatrix} g_x^{\mathrm{ss}} \\ g_y^{\mathrm{ss}} \\ g_z^{\mathrm{ss}} \end{bmatrix} = -\frac{1}{4}A_1 \begin{bmatrix} s_y^{\mathrm{ss}} \\ -s_x^{\mathrm{ss}} \\ 0 \end{bmatrix} - \mathrm{i}\frac{1}{4}A_1 \begin{bmatrix} 0 \\ 0 \\ i_z^{\mathrm{ss}} \end{bmatrix}. \tag{22}
$$

The rate constants pv_- and v_+ needed to calculate the SE enhancement (eq. (5)) are determined from g_z^{ss} using the following equality, which combines (Sezer, 2023a, eq. (31)) and (Sezer, 2023b, eq. (42)):

$$
\dot{i}_z|_{\mathrm{coh}}^{\mathrm{ss}} = -\mathrm{Re}\{\mathrm{i}A_1^* g_z^{\mathrm{ss}}\} = -R_{1I}^A i_z^{\mathrm{ss}} - v_+ i_z^{\mathrm{ss}} - pv_- s_z^{\mathrm{eq}}. \tag{23}
$$

(Re{} takes the real part of its argument.) The term proportional to R_{1I}^A on the right-hand side of (23) accounts for the contribution of the coherences g_i to the nuclear T_1 relaxation in the absence of mw excitation. This contribution should be removed when calculating the mw-related rates v_+ and pv_-.

To a good approximation the electronic spin dynamics is independent from the dipolar interaction with the nuclear spins, as other mechanisms are more efficient in causing electronic relaxation, especially in liquids. As a result, the steady-state expressions from Sec. 3.1 can be used when solving (22) for g_z^{ss}.

Inverting the matrix $\mathbb{B}$ in (22), and using $s_{x,y}^{\mathrm{ss}}$ from before, we find

$$
g_z^{\mathrm{ss}} = \omega_1 \frac{1}{4}A_1([\mathbb{B}^{-1}]_{zx} + \Delta T_2[\mathbb{B}^{-1}]_{zy})P_0^{-1}s_z^{\mathrm{eq}}
$$
$$
- \mathrm{i}\frac{1}{4}A_1[\mathbb{B}^{-1}]_{zz} i_z^{\mathrm{ss}}, \tag{24}
$$

MAGNETIC RESONANCE
Discussions

where $[\mathbb{B}^{-1}]_{ij}$ is the ijth matrix element of $\mathbb{B}^{-1}$. Substituting this g_z^{ss} into (23) we identify the desired SE rate constants

$$R_{1I}^A = \delta^2 \mathrm{Re}\{[\mathbb{B}_{\omega_1=0}^{-1}]_{zz}\}$$

$$v_+ = \delta^2 \mathrm{Re}\{[\mathbb{B}^{-1}]_{zz}\} - R_{1I}^A$$

$$pv_- = -\delta^2 \omega_1 P_0^{-1} \mathrm{Im}\{[\mathbb{B}^{-1}]_{zx} + \Delta T_2 [\mathbb{B}^{-1}]_{zy}\}, \tag{25}$$

where

$$\delta^2 = (A_1^* A_1)/4 \tag{26}$$

reflects the strength of the dipolar interaction. ($\mathrm{Im}\{\}$ takes the imaginary part of its argument.)

In liquids, where A_1 is time-dependent, we will need to modify the matrix $\mathbb{B}^{-1}$ in (25) without changing the structure of these expressions (Sec. 3.3). In the case of solids (i.e., when A_1 does not change with time), it is possible to carry out the inversion of $\mathbb{B}$ by expressing g_x^{ss} and g_z^{ss} in terms of g_y^{ss}, analogously to our treatment of the Bloch equations in the previous subsection.

From the upper and lower rows of $\mathbb{B}$ in (22) we find

$$g_x^{\mathrm{ss}} = -\Delta(R_2 + i\omega_I)^{-1} g_y^{\mathrm{ss}} - \frac{1}{4} A_1 (R_2 + i\omega_I)^{-1} s_y^{\mathrm{ss}}$$

$$g_z^{\mathrm{ss}} = \omega_1 (R_1 + i\omega_I)^{-1} g_y^{\mathrm{ss}} - i\frac{1}{4} A_1 (R_1 + i\omega_I)^{-1} i_z^{\mathrm{ss}}. \tag{27}$$

Substituting this g_z^{ss} into (23) we obtain

$$\dot{i}_z|_{\mathrm{coh}}^{\mathrm{ss}} = -\omega_1 \mathrm{Re}\{i A_1^* (R_1 + i\omega_I)^{-1} g_y^{\mathrm{ss}}\}$$

$$\qquad - \delta^2 \mathrm{Re}\{(R_1 + i\omega_I)^{-1}\} i_z^{\mathrm{ss}}. \tag{28}$$

The first term on the right-hand side of the equality in (28) vanishes when $\omega_1 = 0$. In contrast, the term in the second line is independent of ω_1 and thus contributes also in the absence of mw excitation. We thus identify this second term with the thermal relaxation rate

$$R_{1I}^A = \delta^2 \mathrm{Re}\{(R_1 + i\omega_I)^{-1}\}. \tag{29}$$

Since we are not interested in this rate, the second summand in (28) can be dropped at this stage. The rate constants v_+ and pv_- will thus be identified using only the first line in (28):

$$\omega_1 \mathrm{Re}\{i A_1^* (R_1 + i\omega_I)^{-1} g_y^{\mathrm{ss}}\} = v_+ i_z^{\mathrm{ss}} + pv_- s_z^{\mathrm{eq}}. \tag{30}$$

Substituting g_x^{ss} and g_z^{ss} from (27) into the middle equation in (22), and using the electronic steady state, we find

$$g_y^{\mathrm{ss}} = \frac{1}{4} A_1 \omega_1 \Delta P_0^{-1} [R_2^{-1} + (R_2 + i\omega_I)^{-1}] P^{-1} s_z^{\mathrm{eq}}$$

$$\qquad + i\frac{1}{4} A_1 \omega_1 (R_1 + i\omega_I)^{-1} P^{-1} i_z^{\mathrm{ss}}, \tag{31}$$

where

$$P = R_2 + \mathrm{i}\omega_I + \omega_1^2 (R_1 + \mathrm{i}\omega_I)^{-1} + \Delta^2 (R_2 + \mathrm{i}\omega_I)^{-1} \tag{32}$$

generalizes (14) such that $P_0 = P(\omega_I = 0)$. Finally, using this g_y^{ss} in (30) we obtain

$$v_+ = -\delta^2 \omega_1^2 \, \mathrm{Re} \left\{ \frac{(R_1 + \mathrm{i}\omega_I)^{-2}}{R_2 + \mathrm{i}\omega_I + \frac{\omega_1^2}{R_1 + \mathrm{i}\omega_I} + \frac{\Delta^2}{R_2 + \mathrm{i}\omega_I}} \right\} \tag{33}$$

270 and

$$pv_- = -\delta^2 \omega_1^2 \frac{\Delta}{R_2 + \omega_1^2 T_1 + \Delta^2 T_2}$$
$$\times \mathrm{Im} \left\{ \frac{[R_2^{-1} + (R_2 + \mathrm{i}\omega_I)^{-1}](R_1 + \mathrm{i}\omega_I)^{-1}}{R_2 + \mathrm{i}\omega_I + \frac{\omega_1^2}{R_1 + \mathrm{i}\omega_I} + \frac{\Delta^2}{R_2 + \mathrm{i}\omega_I}} \right\}. \tag{34}$$

In these expressions we have written down the combinations P and P_0 explicitly in order to show in closed form how v_+ and pv_- depend on all parameters. For example, we immediately see that pv_- is odd in the offset Δ while v_+ is even. Because the SE-DNP enhancement is proportional to the ratio of these two rates (eq. (5)), it has the characteristic odd (i.e., antisymmetric)

275 dependence on the offset from the electronic resonance.

When generalizing the SE spin dynamics to g-tensor anisotropy, we will write the dynamical equations (21) as

$$\dot{\vec{g}}(t) = -\mathbb{B}\vec{g}(t) - \frac{1}{4} A_1 \mathbb{G}\vec{s}(t) - \mathrm{i}\frac{1}{4} A_1 \hat{k} i_z(t) \tag{35}$$

with

$$\vec{g}(t) = \begin{bmatrix} g_x(t) \\ g_y(t) \\ g_z(t) \end{bmatrix}, \qquad \mathbb{G} = \begin{bmatrix} 0 & 1 & 0 \\ -1 & 0 & 0 \\ 0 & 0 & 0 \end{bmatrix} = \frac{\partial \mathbb{B}}{\partial \Delta}. \tag{36}$$

280 ### 3.3 Solid effect in liquids

The modulation of the dipolar interaction by translational diffusion was described in Sezer (2023b) on the level of the spectral density of the motional model, which was denoted by $J_{11}(s)$ since this is the Laplace transform of the auto-correlation function of the dipolar interaction A_1 (hence the double subscript of J). As an example, the spectral density of the force-free hard-sphere (FFHS) model of translational diffusion is (Ayant et al., 1975; Hwang and Freed, 1975)

285
$$J_{11}^{\mathrm{ffhs}}(s) = \langle \delta^2 \rangle \tau \frac{(s\tau)^{\frac{1}{2}} + 4}{(s\tau)^{\frac{3}{2}} + 4(s\tau) + 9(s\tau)^{\frac{1}{2}} + 9}. \tag{37}$$

Here, the parameter

$$\tau = b^2 / D_{\mathrm{trans}} \tag{38}$$

11

MAGNETIC
RESONANCE
Open Access
Discussions

is the diffusive time scale of the model, which depends on the contact distance of the electronic and nuclear spins, b, and on the coefficient of their relative translational diffusion, D_{trans}, and

290
$$\langle \delta^2 \rangle = D_{\text{dip}}^2 \frac{6\pi}{5} \frac{N}{3b^3}. \tag{39}$$

is the average of the dipolar interaction strength δ^2 over the sample volume, times the concentration of the electronic spins, N.

It is convenient to write J_{11}, which has units of angular frequency, as

$$J_{11}(s) = \langle \delta^2 \rangle j_{11}(s), \tag{40}$$

where $j_{11}(s)$ has units of time. This factorization confines the effect of the parameters N, b and the constant D_{dip} to the scaling
295 factor $\langle \delta^2 \rangle$. The factor $j_{11}(s)$ then fully accounts for the line shape of the SE-DNP spectrum, which results from the interplay between the offset frequency and the time scale of the translational motion.

According to Sezer (2023b), the modification from solids to liquids amounts to replacing the matrix $\mathbb{B}^{-1}$ in (25) by the matrix

$$\mathbb{Q} = j_{11}(\mathbb{B}), \tag{41}$$

300 and also replacing δ^2 by $\langle \delta^2 \rangle$. The desired SE rate constants in liquids are thus

$$\begin{aligned}
R_{1I}^A &= \langle \delta^2 \rangle \text{Re}\{[\mathbb{Q}_{\omega_1=0}]_{zz}\} \\
v_+ &= \langle \delta^2 \rangle \text{Re}\{[\mathbb{Q}]_{zz}\} - R_{1I}^A \\
pv_- &= -\langle \delta^2 \rangle \omega_1 P_0^{-1} \text{Im}\{[\mathbb{Q}]_{zx} + \Delta T_2 [\mathbb{Q}]_{zy}\}.
\end{aligned} \tag{42}$$

We now clarify the meaning of (41). Following the definition of a function of a matrix, one should first solve the eigenvalue problem of $\mathbb{B}$, i.e., $\mathbb{B}\mathbb{U} = \mathbb{U}\Lambda$, where the diagonal matrix $\Lambda = \text{diag}(\lambda_1, \lambda_2, \lambda_3)$ contains the three eigenvalues and the columns of $\mathbb{U}$ contain the corresponding (right) eigenvectors. Then one should evaluate the spectral density at the three eigenvalues:
305 $\ell_n = j_{11}(\lambda_n)$. Finally, one should form the diagonal matrix $\mathbb{L} = \text{diag}(\ell_1, \ell_2, \ell_3)$ and calculate $\mathbb{Q} = \mathbb{U}\mathbb{L}\mathbb{U}^{-1}$. Comparing this expression of $\mathbb{Q}$ with $\mathbb{B}^{-1} = \mathbb{U}\Lambda\mathbb{U}^{-1}$ we see that in the transition from solids to liquids, where $\mathbb{B}^{-1}$ is replaced by $\mathbb{Q}$, we essentially "process" the eigenvalues of $\mathbb{B}$ with the spectral density function j_{11}. This step prevents us from eliminating the variables $g_{x,z}^{\text{ss}}$ the way we did previously for solids (Sec. 3.2). Because of that, the rate constants in liquids (eq. (42)) need to be calculated numerically.

310 Nonetheless, it is still possible to simplify the expression for R_{1I}^A since when $\omega_1 = 0$ the zz component of $\mathbb{B}$ is decoupled from the rest of the matrix. One then finds

$$R_{1I}^A = \langle \delta^2 \rangle \text{Re}\{j_{11}(R_1 + i\omega_I)\}. \tag{43}$$

Clearly, the time-dependence of the dipolar interaction modifies all rate constants, including R_{1I}^A (*cf.* eq. (29)).

4 Slow-motional EPR and DNP spectra for anisotropic g tensor

In this section we show how to account for g-tensor anisotropies when the tumbling of the radical is slow. Because our description of SE is built around the Bloch equations (Sezer, 2023a, b), we first adapt the pioneering approach of Freed et al. (1971) to our needs (Secs. 4.1, 4.2 and 4.3) and then generalize it to SE-DNP (Secs. 4.4 and 4.5).

4.1 Stochastic Liouville equation

Following Freed et al. (1971), we account for the effect of tumbling on the EPR spectrum using the SLE formalism (Anderson, 1954; Kubo, 1954). We describe the rotational state of the radical statistically with the probability density $P(\Omega, t)$, which quantifies the likelihood that at time t the molecular system of coordinates attached to the radical has orientation Ω with respect to the laboratory system of axes. This probability evolves with the Fokker-Planck equation

$$\frac{\partial}{\partial t} p(\Omega, t | \Omega_0, t_0) = D_{\mathrm{rot}} \nabla_\Omega^2 p(\Omega, t | \Omega_0, t_0), \tag{44}$$

where D_{rot} is the rotational diffusion constant of the radical and the Laplacian differential operator ∇_Ω^2 acts on the orientation variable Ω. The operator

$$K_\Omega = -D_{\mathrm{rot}} \nabla_\Omega^2 \tag{45}$$

satisfies the following eigenvalue problem

$$K_\Omega \mathscr{D}_{mn}^\ell(\Omega) = D_{\mathrm{rot}} \ell(\ell+1) \mathscr{D}_{mn}^\ell(\Omega), \tag{46}$$

where the eigenfunctions $\mathscr{D}_{mn}^\ell(\Omega)$ are the Wigner rotation matrix elements, which are orthogonal to each other:

$$\int \mathscr{D}_{MN}^{L*}(\Omega) \mathscr{D}_{mn}^\ell(\Omega) \mathrm{d}\Omega = \frac{8\pi^2}{2L+1} \delta_{L\ell} \delta_{Mm} \delta_{Nn}. \tag{47}$$

From (46) it is clear that the time derivative on the left-hand side of (44) vanishes for the equilibrium probability

$$p^{\mathrm{eq}}(\Omega) = \frac{1}{8\pi^2} = \frac{1}{8\pi^2} \mathscr{D}_{00}^0(\Omega). \tag{48}$$

In the presence of g-tensor anisotropy, the electronic Larmor frequency depends on the orientation Ω of the radical as follows:[4]

$$\omega(\Omega) = \omega_0 + \gamma_0^2 \mathscr{D}_{00}^2(\Omega) + \gamma_2^2 [\mathscr{D}_{-20}^2(\Omega) + \mathscr{D}_{20}^2(\Omega)], \tag{49}$$

where the angular frequencies

$$\gamma_0^2 = \frac{2}{3} \left[g_{zz} - \frac{1}{2}(g_{xx} + g_{yy}) \right] \mu_{\mathrm{B}} B_0 / \hbar$$

$$\gamma_2^2 = \frac{1}{\sqrt{6}} (g_{xx} - g_{yy}) \mu_{\mathrm{B}} B_0 / \hbar \tag{50}$$

---

[4]We follow Freed et al. (1971) and consider the effect of the g-tensor anisotropy only on the secular terms in the electronic spin Hamiltonian, i.e., those proportional to the spin operator S_z. The response of the non-secular terms to the g anisotropy is neglected.

MAGNETIC
RESONANCE
Discussions

are formed from the components g_{xx}, g_{yy} and g_{zz} of the g-tensor in the molecular frame.

Because the electronic Larmor frequency depends on Ω, the offset frequency Δ also becomes a function of the molecular

340 orientation. As an example, for a fixed Ω the Bloch equations (17) should be modified as

$$\dot{\vec{s}}(t) = -[\mathbb{B}_0 + \mathbb{F}(\Omega)]\vec{s}(t) + R_1\hat{k}s_z^{\text{eq}}, \tag{51}$$

where the orientation dependence is confined to the 3×3 matrix

$$\mathbb{F}(\Omega) = \left\{ \gamma_0^2 \mathscr{D}_{00}^2(\Omega) + \gamma_2^2 [\mathscr{D}_{-20}^2(\Omega) + \mathscr{D}_{20}^2(\Omega)] \right\} \mathbb{G}. \tag{52}$$

(The matrix $\mathbb{G}$ was introduced in (36).) It should be stressed, however, that (51) is not a legitimate equation of motion, as it

345 does not account for the dynamics of the orientation Ω.

The SLE formalism remedies this deficiency by introducing the orientation-conditioned averages $\vec{s}(\Omega, t)$, whose spatial part

evolves according to the Bloch equations (51) and whose Ω dependence evolves according to the diffusion equation (44):

$$\frac{\partial}{\partial t}\vec{s}(\Omega, t) = -(K_\Omega \otimes \mathbb{E} + E_\Omega \otimes \mathbb{B}_0)\vec{s}(\Omega, t)$$

$$- E_\Omega \otimes \mathbb{F}(\Omega)\vec{s}(\Omega, t) + R_1\hat{k}s_z^{\text{eq}}p^{\text{eq}}(\Omega). \tag{53}$$

Here $\mathbb{E}$ is the 3×3 identity matrix in 3D space and E_Ω is the identity operator in the same abstract space as K_Ω. The outer

350 product $\otimes$ is needed to create a combined operator that acts simultaneously in both of these spaces.

Since the functions $\mathscr{D}_{mn}^\ell(\Omega)$ form a complete set, we expand $\vec{s}(\Omega, t)$ as follows:

$$\vec{s}(\Omega, t) = \frac{1}{8\pi^2} \sum_{\ell=0}^\infty \sum_{m=-\ell}^\ell \sum_{n=-\ell}^\ell \mathscr{D}_{mn}^\ell(\Omega)\vec{s}_{mn}^\ell(t). \tag{54}$$

The coefficients $\vec{s}_{mn}^\ell$, which contain the time-dependence, can be obtained from $\vec{s}(\Omega, t)$ using the orthogonality of $\mathscr{D}_{mn}^\ell(\Omega)$

(eq. (47)):

355 $$\vec{s}_{MN}^L(t) = (2L+1)\int \mathscr{D}_{MN}^{L*}(\Omega)\vec{s}(\Omega, t)\,\mathrm{d}\Omega. \tag{55}$$

Ultimately, the only property that we care about is the integral of the SLE variable $\vec{s}(\Omega, t)$ over all orientations:

$$\int \vec{s}(\Omega, t)\,\mathrm{d}\Omega = \int \mathscr{D}_{00}^0(\Omega)\vec{s}(\Omega, t)\,\mathrm{d}\Omega = \vec{s}_{00}^0(t). \tag{56}$$

In that sense, the (vector) coefficient $\vec{s}_{00}^0(t)$ is the main object of interest, while all other coefficients $\vec{s}_{mn}^\ell(t)$ play an auxiliary,

book-keeping role.

360 Substituting $\vec{s}(\Omega, t)$ from (54) into (53), multiplying both sides by $\mathscr{D}_{MN}^{L*}(\Omega)$ and integrating over Ω, we get

$$\dot{\vec{s}}_{MN}^L(t) = R_1\hat{k}s_z^{\text{eq}}\delta_{L0}\delta_{M0}\delta_{N0}$$

$$- [D_{\text{rot}}L(L+1) + \mathbb{B}_0]\vec{s}_{MN}^L(t)$$

$$- \sum_{\ell mn} \left(\frac{2L+1}{8\pi^2} \int \mathscr{D}_{MN}^{L*}(\Omega)\mathscr{D}_{mn}^\ell(\Omega)\mathbb{F}(\Omega)\mathrm{d}\Omega \right) \vec{s}_{mn}^\ell(t). \tag{57}$$

14

**MAGNETIC
RESONANCE**
Open Access
Discussions

Clearly, the terms proportional to K_Ω and $\mathbb{B}_0$ in the SLE (53) do not mix coefficients $\vec{s}_{MN}^L$ with different values of L, M and N. In other words, these two operators are diagonal in the selected representation. The term proportional to $\mathbb{F}(\Omega)$, on the other hand, mixes coefficients with different L and M (but not N, as we discuss below).

365   The integral in the last line of (57) contains the product of three Wigner rotation matrix elements. These can be expressed in therms of the Clebsch-Gordan coefficients $C_{\ell_1 m_1 \ell_2 m_2}^{LM}$. Specifically, for the $\mathscr{D}_{K0}^2(\Omega)$ in eq. (52), we have

$$\frac{2L+1}{8\pi^2} \int \mathscr{D}_{MN}^{L*}(\Omega) \mathscr{D}_{K0}^2(\Omega) \mathscr{D}_{mn}^\ell(\Omega) \mathrm{d}\Omega = C_{2K\ell m}^{LM} C_{20\ell n}^{LN}, \tag{58}$$

which leads to

$$\dot{\vec{s}}_{MN}^L(t) = R_1 \hat{k} s_z^{\mathrm{eq}} \delta_{L0} \delta_{M0} \delta_{N0}$$
$$- [D_{\mathrm{rot}} L(L+1) + \mathbb{B}_0] \vec{s}_{MN}^L(t)$$
$$- \sum_{\ell mn} [\gamma_0^2 C_{20\ell m}^{LM} + \gamma_2^2 (C_{2-2\ell m}^{LM} + C_{22\ell m}^{LM})] C_{20\ell n}^{LN} \mathbb{G} \vec{s}_{mn}^\ell(t). \tag{59}$$

370   In (59), the sum over ℓ mixes only expansion coefficients whose values ℓ differ by two from L, in both the positive and negative directions, because all three Wigner rotation matrix elements in $\mathbb{F}$ have $L = 2$ (eq. (52)). Since we need $\vec{s}_{00}^0$ at the end, it is sufficient to consider only coefficients with even values of ℓ. Furthermore, as the Wigner rotation matrix elements in $\mathbb{F}$ have $M = 0, \pm 2$ and $N = 0$, the sum over m mixes only coefficients whose values m are either equal to M or differ from it by two units, while the sum over n does not mix any coefficients with n different from N. These considerations imply that the

375   triple sum in (59) will go only over $\vec{s}_{m0}^\ell$ with even ℓ and m. Finally, because the Wigner rotation matrix elements with $M = 2$ and $M = -2$ appear in a symmetrical way in $\mathbb{F}$, it becomes possible to work with the symmetrized coefficients (Freed et al., 1971)

$$\vec{s}^{LM} = \frac{1}{2}(\vec{s}_{-M0}^L + \vec{s}_{M0}^L), \tag{60}$$

thus restricting M to non-negative values ($0 \leqslant M \leqslant L$). The lowest-order coefficients that are coupled by the SLE dynamics

380   are thus $\vec{s}^{00}$, $\vec{s}^{20}$, $\vec{s}^{22}$, $\vec{s}^{40}$, $\vec{s}^{42}$, $\vec{s}^{44}$, $\vec{s}^{60}$, etc.

4.2 Matrix representation of the SLE dynamics

While the above considerations greatly reduce the needed coefficients, there is still an infinite number left. In any practical work, this infinite set is truncated by selecting a maximum value of L to account for, and setting to zero the coefficients with $L > L_{\max}$. Since the total number of even L such that $L \leqslant L_{\max}$ is $n_L = L_{\max}/2 + 1$, the total number of remaining

385   coefficients $\vec{s}^{LM}$ is $n_{\mathrm{tot}} = n_L(n_L + 1)/2 = L_{\max}^2/8 + 3L_{\max}/4 + 1$. For the smallest non-trivial choice of $L_{\max} = 2$, $n_{\mathrm{tot}} = 3$ (with $\vec{s}^{00}$, $\vec{s}^{20}$ and $\vec{s}^{22}$). The number of coefficients increases quadratically with $L_{\max}$ (e.g., $n_{\mathrm{tot}} = 15, 28, 45$ for $L_{\max} = 8, 12, 16$, respectively).

To compactly write down how these coefficients are mixed by the SLE dynamics, we introduce the following abstract vectors with n_{tot} elements:

$$
390 \quad \mathbf{1}^{00} = \begin{bmatrix} 1 \\ 0 \\ 0 \\ \vdots \end{bmatrix}, \qquad \boldsymbol{s}_i(t) = \begin{bmatrix} s_i^{00}(t) \\ s_i^{20}(t) \\ s_i^{22}(t) \\ \vdots \end{bmatrix} \quad (i = x, y, z), \tag{61}
$$

where the former is needed for the first term on the right-hand side of (59). The SLE dynamics then becomes

$$
\begin{bmatrix} \dot{\boldsymbol{s}}_x(t) \\ \dot{\boldsymbol{s}}_y(t) \\ \dot{\boldsymbol{s}}_z(t) \end{bmatrix} = -\mathcal{B}_0 \begin{bmatrix} \boldsymbol{s}_x(t) \\ \boldsymbol{s}_y(t) \\ \boldsymbol{s}_z(t) \end{bmatrix} + R_1 \begin{bmatrix} 0 \\ 0 \\ \mathbf{1}^{00} \end{bmatrix} s_z^{\text{eq}}, \tag{62}
$$

where

$$
\mathcal{B}_0 = \begin{bmatrix} \mathbf{R}_2 & \boldsymbol{\Delta} & 0 \\ -\boldsymbol{\Delta} & \mathbf{R}_2 & \omega_1 \mathbf{E} \\ 0 & -\omega_1 \mathbf{E} & \mathbf{R}_1 \end{bmatrix} \tag{63}
$$

395 is a $3n_{\text{tot}} \times 3n_{\text{tot}}$ matrix, and $\mathbf{E}$, $\mathbf{R}_1$, $\mathbf{R}_2$ and $\boldsymbol{\Delta}$ are $n_{\text{tot}} \times n_{\text{tot}}$ matrices.

The first three of these sub-matrices are purely diagonal: $\mathbf{E}$ is the identity matrix and

$$
\mathbf{R}_{1,2} = R_{1,2}\mathbf{E} + D_{\text{rot}}\mathbf{C}_D, \tag{64}
$$

with the diagonal elements of $\mathbf{C}_D$ being equal to $L(L+1)$. For the simplest case of $L_{\max} = 2$ with only three coefficients ($\vec{s}^{00}$, $\vec{s}^{20}$ and $\vec{s}^{22}$),

$$
400 \quad \mathbf{E} = \begin{bmatrix} 1 & & \\ & 1 & \\ & & 1 \end{bmatrix}, \qquad \mathbf{C}_D = \begin{bmatrix} 0 & & \\ & 6 & \\ & & 6 \end{bmatrix}. \tag{65}
$$

In (63), the diagonal matrices $\mathbf{R}_{1,2}$ and $\mathbf{E}$, which originate from the second line in (59), do not mix coefficients with different L and M. Only the sub-matrix $\boldsymbol{\Delta}$, which is of the form

$$
\boldsymbol{\Delta} = \Delta\mathbf{E} + \gamma_0^2\mathbf{C}_0 + \gamma_2^2\mathbf{C}_2, \tag{66}
$$

mixes coefficients of different orders. In fact, the mixing is due to the matrices $\mathbf{C}_{0,2}$, which modify the frequency offset Δ in

405 proportion to the g-tensor anisotropies γ_0^2 and γ_2^2. For $L_{\max} = 2$,

$$
\mathbf{C}_0 = \begin{bmatrix} 0 & \frac{1}{5} & 0 \\ 1 & \frac{2}{7} & 0 \\ 0 & 0 & -\frac{2}{7} \end{bmatrix}, \qquad \mathbf{C}_2 = \begin{bmatrix} 0 & 0 & \frac{1}{5} \times 2 \\ 0 & 0 & -\frac{2}{7} \times 2 \\ 1 & -\frac{2}{7} & 0 \end{bmatrix}. \tag{67}
$$

MAGNETIC RESONANCE
Discussions

(The factors of two in the last column of $\mathbf{C}_2$ arise from the fact that coefficients with $M = 0$ pose an exception to the symmetrization (60).) The matrix elements of these two matrices in the most general case are

$$[\mathbf{C}_0]_{LM,\ell m} = C_{20\ell m}^{LM} C_{20\ell 0}^{L0}$$

$$[\mathbf{C}_2]_{LM,\ell m} = (C_{2-2\ell m}^{LM} + C_{22\ell m}^{LM} + \delta_{M0} C_{22\ell m}^{LM}) C_{20\ell 0}^{L0}, \tag{68}$$

where the summand proportional to δ_{M0} in the second line accounts for the factor of two that is needed by the coefficients $\vec{s}^{L0}$.

Selecting $L_{\max} = 0$ in the above formalism amounts to retaining only the (3D vector) coefficient $\vec{s}^{00}$. Then the matrix $\mathcal{B}_0$ in (63) reduces to $\mathbb{B}_0$, and (62) reduces to the classical Bloch equations for a homogeneous line. For $L_{\max} > 0$, the diagonal matrices $\mathbf{R}_1$ and $\mathbf{R}_2$ cause the coefficients s_z^{LM} and $s_{x,y}^{LM}$, respectively, to decay exponentially, with those with larger L being suppressed more strongly by the tumbling. Analogously to the Bloch equations, the mw excitation mixes the y and z components of $\vec{s}^{LM}$, without mixing their LM dependence. The latter is mixed only by the offset matrix $\boldsymbol{\Delta}$, as elaborated above.

By building the SLE dynamics on top of the classical Bloch equations, we have arrived at a rather intuitive picture of how the g-tensor anisotropy is incorporated into the spin dynamics. Specifically, every element of the Bloch matrix $\mathbb{B}_0$ (eq. (19) with $\omega_I = 0$) is replaced by a matrix in the space of LM indices (eq. (63)). In this replacement, all elements except the frequency offset become diagonal matrices in the LM space, with the mixing in this space being entirely due to the offset. Since we describe the solid effect by two coupled Bloch equations, this intuition about the effect of g-tensor anisotropy on the spin dynamics will be helpful when adapting the approach to SE-DNP.

4.3 EPR spectrum

The cw-EPR spectrum and the electronic saturation factor under g-tensor anisotropy are obtained from the steady state of (62),

$$\mathcal{B}_0 \begin{bmatrix} \boldsymbol{s}_x^{\mathrm{ss}} \\ \boldsymbol{s}_y^{\mathrm{ss}} \\ \boldsymbol{s}_z^{\mathrm{ss}} \end{bmatrix} = R_1 \begin{bmatrix} 0 \\ 0 \\ \mathbf{1}^{00} \end{bmatrix} s_z^{\mathrm{eq}}, \tag{69}$$

which can be solved by inverting the $3n_{\mathrm{tot}} \times 3n_{\mathrm{tot}}$ matrix $\mathcal{B}_0$ numerically. However, it is also possible to solve (69) by inverting a single matrix with dimensions that are three times smaller (i.e., $n_{\mathrm{tot}} \times n_{\mathrm{tot}}$), as we show next.

First, taking advantage of the zeros in $\mathcal{B}_0$ (eq. (63)), we express $\boldsymbol{s}_x^{\mathrm{ss}}$ and $\boldsymbol{s}_z^{\mathrm{ss}}$ in terms of $\boldsymbol{s}_y^{\mathrm{ss}}$:

$$\boldsymbol{s}_x^{\mathrm{ss}} = -\mathbf{R}_2^{-1} \boldsymbol{\Delta} \, \boldsymbol{s}_y^{\mathrm{ss}}$$

$$\boldsymbol{s}_z^{\mathrm{ss}} = \omega_1 \mathbf{R}_1^{-1} \boldsymbol{s}_y^{\mathrm{ss}} + R_1 \mathbf{R}_1^{-1} \mathbf{1}^{00} s_z^{\mathrm{eq}}. \tag{70}$$

Because only the first element of $\mathbf{1}^{00}$ is non-zero, and the diagonal matrix $\mathbf{R}_1$ does not mix coefficients with different values of LM, the second equality in (70) becomes

$$\boldsymbol{s}_z^{\mathrm{ss}} = \omega_1 \mathbf{R}_1^{-1} \boldsymbol{s}_y^{\mathrm{ss}} + \mathbf{1}^{00} s_z^{\mathrm{eq}}. \tag{71}$$

For the 00th (i.e., first) element of $\boldsymbol{s}_z^{\mathrm{ss}}$ we thus have $s_z^{00} = \omega_1 T_1 s_y^{00} + s_z^{\mathrm{eq}}$, which is identical to the second equality in (12). We thus conclude that the proportionality between the electronic saturation factor and the in-phase EPR line shape (eq. (16)) is not limited to a homogenous line but applies also under g-tensor anisotropy.

Second, from the middle row of the matrix $\mathcal{B}_0$ (eq. (63)), and after substituting $\boldsymbol{s}_x^{\mathrm{ss}}$ and $\boldsymbol{s}_z^{\mathrm{ss}}$ from (70), we find

$$\boldsymbol{s}_y^{\mathrm{ss}} = -\omega_1 \mathbf{P}_0^{-1} \mathbf{1}^{00} s_z^{\mathrm{eq}}, \tag{72}$$

where we have introduced the $n_{\mathrm{tot}} \times n_{\mathrm{tot}}$ matrix

$$\mathbf{P} = (\mathbf{R}_2 + \mathrm{i}\omega_I) + \omega_1^2 (\mathbf{R}_1 + \mathrm{i}\omega_I)^{-1} + \boldsymbol{\Delta}(\mathbf{R}_2 + \mathrm{i}\omega_I)^{-1}\boldsymbol{\Delta} \tag{73}$$

and $\mathbf{P}_0 = \mathbf{P}(\omega_I = 0)$. The matrix $\mathbf{P}_0$ generalizes P_0 (eq. (14)) and (72) generalizes (13) to the case of g-tensor anisotropy.

From the 00th components of $\boldsymbol{s}_y^{\mathrm{ss}}$ and $\boldsymbol{s}_x^{\mathrm{ss}}$ we find

$$\mathrm{abs} = -\omega_1 [\mathbf{P}_0^{-1}]_{11}, \qquad \mathrm{dsp} = \omega_1 T_2 [\boldsymbol{\Delta} \mathbf{P}_0^{-1}]_{11}, \tag{74}$$

where we used the fact that $\mathbf{R}_2$ is a diagonal matrix. These expressions generalize eqs. (15) to the case of g-tensor anisotropy. The corresponding saturation factor as a function of the offset is then (from eqs. (16) and (74))

$$s(\Delta) = \omega_1^2 T_1 [\mathbf{P}_0^{-1}(\Delta)]_{11}. \tag{75}$$

As claimed, to solve for the steady state numerically we need to invert the matrix $\mathbf{P}_0$ whose dimensions are three times smaller than those of $\mathcal{B}_0$. (The two matrix inversions needed to calculate $\mathbf{P}_0$ itself involve the diagonal matrices $\mathbf{R}_{1,2}$.)

The cw-EPR spectrum in derivative mode can be calculated from the derivative of $\mathbf{P}_0$ with respect to the (scalar) frequency offset Δ:

$$\frac{\partial \mathbf{P}_0}{\partial \Delta} = \mathbf{R}_2^{-1} \boldsymbol{\Delta} + \boldsymbol{\Delta} \mathbf{R}_2^{-1}. \tag{76}$$

The in-phase and out-of-phase derivative spectra are then obtained from the first (i.e., 00th) components of the vectors

$$\frac{\partial \boldsymbol{s}_y}{\partial \Delta} = \omega_1 \mathbf{P}_0^{-1} (\mathbf{R}_2^{-1}\boldsymbol{\Delta} + \boldsymbol{\Delta}\mathbf{R}_2^{-1}) \mathbf{P}_0^{-1} \mathbf{1}^{00} s_z^{\mathrm{eq}}$$
$$\frac{\partial \boldsymbol{s}_x}{\partial \Delta} = -\mathbf{R}_2^{-1} (\boldsymbol{s}_y + \boldsymbol{\Delta} \frac{\partial \boldsymbol{s}_y}{\partial \Delta}). \tag{77}$$

These expressions are used in Sec. 5 to fit the experimental EPR spectra from fig. 1.

In fig. 2 we show examples of (integral) EPR spectra calculated using the presented approach for different tumbling times τ_{rot}. The different columns in the figure correspond to different choices of $L_{\max}$. The g-tensor values used in the simulations are characteristic of nitroxide spin labels. We also selected a small mw magnetic field ($B_1 = 0.02\,\mathrm{G}$) to mimic the low-power conditions typical for cw-EPR. The main message of this figure is that slower tumbling requires larger $L_{\max}$. At the same time, we see that $L_{\max} = 8$ is already good enough for $\tau_{\mathrm{rot}} \leqslant 10\,\mathrm{ns}$, which is the range of rotational time scales of relevance to our experimental data (Sec. 5). By selecting $L_{\max} = 10$, to be on the safe side, we only need to invert a 21×21 matrix at every frequency offset, which makes the calculation of g-broadened EPR spectra very fast. This allows us to perform an automated search over the various parameters and fit the experimental cw-EPR spectra in less than a minute.
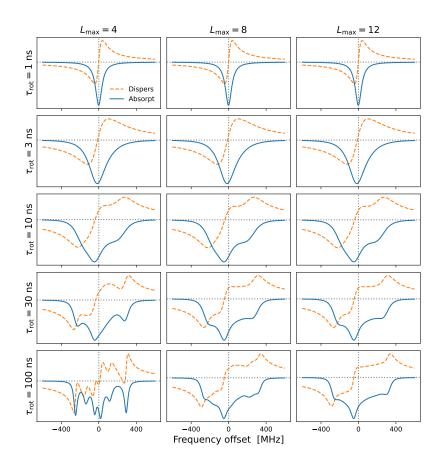
MAGNETIC
RESONANCE
Discussions

Figure 2. Continuous-wave EPR spectra for $g = \mathrm{diag}(2.00755, 2.00555, 2.0023)$ and different tumbling times τ_{rot}. Larger L_{max} is necessary for slower tumbling. The needed L_{max} also depends on the anisotropies, which are $(\gamma_0, \gamma_2) = (-373, 107)$ MHz for $B_0 = 9.403$ T. Other simulation parameters were $B_1 = 0.02$ G, $T_1 = 100$ ns, $T_2^{\mathrm{homog}} = 20$ ns.

4.4 Solid effect in 'solids'

Extending the above treatment to SE-DNP, we combine the spin dynamics in (35) with the rotational dynamics in (44) to form
465 the following SLE:

$$
\frac{\partial}{\partial t}\vec{g}(\Omega, t) = -(K_\Omega \otimes \mathbb{E} + E_\Omega \otimes \mathbb{B})\vec{g}(\Omega, t)
$$
$$
- E_\Omega \otimes \mathbb{F}(\Omega)\vec{g}(\Omega, t)
$$
$$
- \frac{1}{4}A_1 \mathbb{G}\vec{s}(\Omega, t) - \mathrm{i}\frac{1}{4}A_1 \hat{k} i_z(t) p^{\mathrm{eq}}(\Omega). \tag{78}
$$

As before, we introduce the expansion

$$
\vec{\mathcal{g}}(\Omega, t) = \frac{1}{8\pi^2}\sum_{\ell=0}^{\infty}\sum_{m=-\ell}^{\ell}\mathscr{D}_{m0}^2(\Omega)\,\vec{g}_{m0}^\ell(t), \tag{79}
$$

where we have set $n = 0$ from the start, and find

$$
\begin{aligned}
\dot{\vec{g}}^L_{M0}(t) = &-[D_{\mathrm{rot}}L(L+1) + \mathbb{B}]\vec{g}^L_{M0}(t) \\
&- \sum_{\ell m}[\gamma_0^2 C^{LM}_{20\ell m} + \gamma_2^2(C^{LM}_{2-2\ell m} + C^{LM}_{22\ell m})]C^{L0}_{20\ell n}\mathbb{G}\vec{g}^\ell_{m0}(t)
\end{aligned}
$$

470
$$
- \frac{1}{4}A_1\mathbb{G}\,\vec{s}^L_{M0}(t) - \mathrm{i}\frac{1}{4}A_1\hat{k}\,i_z(t)\delta_{L0}\delta_{M0}. \tag{80}
$$

Again, we switch to the symmetrized coefficients

$$
\vec{g}^{LM} = \frac{1}{2}(\vec{g}^L_{-M0} + \vec{g}^L_{M0}) \tag{81}
$$

and form the following three, n_{tot}-dimensional vectors from the spatial components of the 3D vectors $\vec{g}^{LM}$:

$$
\boldsymbol{g}_i = \begin{bmatrix} g^{00}_i \\ g^{20}_i \\ g^{22}_i \\ \vdots \end{bmatrix} \qquad (i = x, y, z). \tag{82}
$$

475   The steady state of the resulting spin dynamics is then

$$
\mathcal{B}\begin{bmatrix} \boldsymbol{g}^{\mathrm{ss}}_x \\ \boldsymbol{g}^{\mathrm{ss}}_y \\ \boldsymbol{g}^{\mathrm{ss}}_z \end{bmatrix} = -\frac{1}{4}A_1\begin{bmatrix} \boldsymbol{s}^{\mathrm{ss}}_y \\ -\boldsymbol{s}^{\mathrm{ss}}_x \\ 0 \end{bmatrix} - \mathrm{i}\frac{1}{4}A_1\begin{bmatrix} 0 \\ 0 \\ \boldsymbol{1}^{00} \end{bmatrix}i^{\mathrm{ss}}_z, \tag{83}
$$

where

$$
\mathcal{B} = \mathcal{B}_0 + \mathrm{i}\omega_I \tag{84}
$$

generalizes the matrix $\mathcal{B}_0$ from (63).

480   Our goal is to solve for $\boldsymbol{g}^{\mathrm{ss}}_z$ since its 00th component should be used in (23) to calculate the rate constants pv_- and v_+. After inverting $\mathcal{B}$ in (83) we find

$$
\begin{aligned}
\boldsymbol{g}^{\mathrm{ss}}_z = &-\frac{1}{4}A_1[\mathcal{B}^{-1}]_{zx}\boldsymbol{s}^{\mathrm{ss}}_y - \frac{1}{4}A_1[\mathcal{B}^{-1}]_{zy}(-\boldsymbol{s}^{\mathrm{ss}}_x) \\
&- \mathrm{i}\frac{1}{4}A_1[\mathcal{B}^{-1}]_{zz}\boldsymbol{1}^{00}i^{\mathrm{ss}}_z.
\end{aligned} \tag{85}
$$

Note that now $[\mathcal{B}^{-1}]_{ij}$ denotes the $n_{\mathrm{tot}} \times n_{\mathrm{tot}}$ sub-matrix of $\mathcal{B}^{-1}$ at position ij, and not a scalar matrix element. Using $\boldsymbol{s}^{\mathrm{ss}}_{x,y}$ from the previous subsection, we find that the first component of $\boldsymbol{g}^{\mathrm{ss}}_z$ is

$$
\begin{aligned}
g^{00}_z = &\omega_1\frac{1}{4}A_1[([\mathcal{B}^{-1}]_{zx} + [\mathcal{B}^{-1}]_{zy}\mathbf{R}_2^{-1}\boldsymbol{\Delta})\mathbf{P}_0^{-1}]_{11}s^{\mathrm{eq}}_z
\end{aligned}
$$

485
$$
- \mathrm{i}\frac{1}{4}A_1[[\mathcal{B}^{-1}]_{zz}]_{11}i^{\mathrm{ss}}_z. \tag{86}
$$

Substituting this result into (23) we obtain

$$R_{1I}^A = \delta^2 \mathrm{Re}\{[[\mathcal{B}_{\omega_1=0}^{-1}]_{zz}]_{11}\}$$
$$v_+ = \delta^2 \mathrm{Re}\{[[\mathcal{B}^{-1}]_{zz}]_{11}\} - R_{1I}^A$$
$$pv_- = -\delta^2\omega_1\mathrm{Im}\{[([\mathcal{B}^{-1}]_{zx} + [\mathcal{B}^{-1}]_{zy}\mathbf{R}_2^{-1}\boldsymbol{\Delta})\mathbf{P}_0^{-1}]_{11}\}. \tag{87}$$

These expressions, which require the inversion of the $3n_{\mathrm{tot}} \times 3n_{\mathrm{tot}}$ matrix $\mathcal{B}$, are directly generalizable to liquids (Sec. 4.5). In 'solids', it is possible to obtain alternative expressions that require the inversion of a smaller, $n_{\mathrm{tot}} \times n_{\mathrm{tot}}$ matrix. To this end,
490   we express $\boldsymbol{g}_x^{\mathrm{ss}}$ and $\boldsymbol{g}_z^{\mathrm{ss}}$ in terms of $\boldsymbol{g}_y^{\mathrm{ss}}$ using the first and last rows of $\mathcal{B}$:

$$\boldsymbol{g}_x^{\mathrm{ss}} = -(\mathbf{R}_2 + \mathrm{i}\omega_I)^{-1}\boldsymbol{\Delta}\boldsymbol{g}_y^{\mathrm{ss}} - \frac{1}{4}A_1(\mathbf{R}_2 + \mathrm{i}\omega_I)^{-1}\boldsymbol{s}_y^{\mathrm{ss}}$$
$$\boldsymbol{g}_z^{\mathrm{ss}} = \omega_1(\boldsymbol{R}_1 + \mathrm{i}\omega_I)^{-1}\boldsymbol{g}_y^{\mathrm{ss}} - \mathrm{i}\frac{1}{4}A_1(\boldsymbol{R}_1 + \mathrm{i}\omega_I)^{-1}\mathbf{1}^{00}i_z^{\mathrm{ss}}. \tag{88}$$

Substituting the first (i.e., 00th) component of $\boldsymbol{g}_z^{\mathrm{ss}}$ in (23) we find

$$R_{1I}^A = \delta^2 \mathrm{Re}\{[(\boldsymbol{R}_1 + \mathrm{i}\omega_I)^{-1}]_{11}\}. \tag{89}$$

Because $\mathbf{R}_1$ is a diagonal matrix, this result is identical to (29), showing that R_{1I}^A is not affected by the anisotropy of the g
495   tensor.

Similarly, from the middle part of $\mathcal{B}$ we obtain

$$\mathbf{P}\boldsymbol{g}_y^{\mathrm{ss}} = \frac{1}{4}A_1[\boldsymbol{s}_x^{\mathrm{ss}} - \boldsymbol{\Delta}(\mathbf{R}_2 + \mathrm{i}\omega_I)^{-1}\boldsymbol{s}_y^{\mathrm{ss}}]$$
$$+ \omega_1\mathrm{i}\frac{1}{4}A_1(\boldsymbol{R}_1 + \mathrm{i}\omega_I)^{-1}\mathbf{1}^{00}i_z^{\mathrm{ss}}. \tag{90}$$

We first observe that $(\mathbf{R}_1 + \mathrm{i}\omega_I)^{-1}\mathbf{1}^{00} = \mathbf{1}^{00}(R_1 + \mathrm{i}\omega_I)^{-1}$ because $\mathbf{R}_1$ is diagonal. Then we substitute $\boldsymbol{s}_{x,y}^{\mathrm{ss}}$ from before to get

$$\boldsymbol{g}_y^{\mathrm{ss}} = \omega_1\frac{1}{4}A_1\mathbf{P}^{-1}[\mathbf{R}_2^{-1}\boldsymbol{\Delta} + \boldsymbol{\Delta}(\mathbf{R}_2 + \mathrm{i}\omega_I)^{-1}]\mathbf{P}_0^{-1}\mathbf{1}^{00}s_z^{\mathrm{eq}}$$
500    $$+ \omega_1\mathrm{i}\frac{1}{4}A_1\mathbf{P}^{-1}\mathbf{1}^{00}(R_1 + \mathrm{i}\omega_I)^{-1}i_z^{\mathrm{ss}}. \tag{91}$$

Finally, substituting the 00th element of $\boldsymbol{g}_y^{\mathrm{ss}}$ in (30) we find

$$v_+ = -\delta^2\omega_1^2\mathrm{Re}\{(R_1 + \mathrm{i}\omega_I)^{-2}[\mathbf{P}^{-1}]_{11}\}$$
$$pv_- = -\delta^2\omega_1^2\mathrm{Im}\{(R_1 + \mathrm{i}\omega_I)^{-1}$$
$$\times [\mathbf{P}^{-1}(\mathbf{R}_2^{-1}\boldsymbol{\Delta} + \boldsymbol{\Delta}(\mathbf{R}_2 + \mathrm{i}\omega_I)^{-1})\mathbf{P}_0^{-1}]_{11}\}. \tag{92}$$

Observe how these expressions generalize (33) and (34) to the case of g-tensor anisotropy.

In the last two rows of fig. 3 we show v_+/δ^2 and pv_-/δ^2, which have units of time. Although the electronic non-saturation
505   factor p and the rate constant v_- always appear together as pv_-, it is helpful to separate these two factors when rationalizing
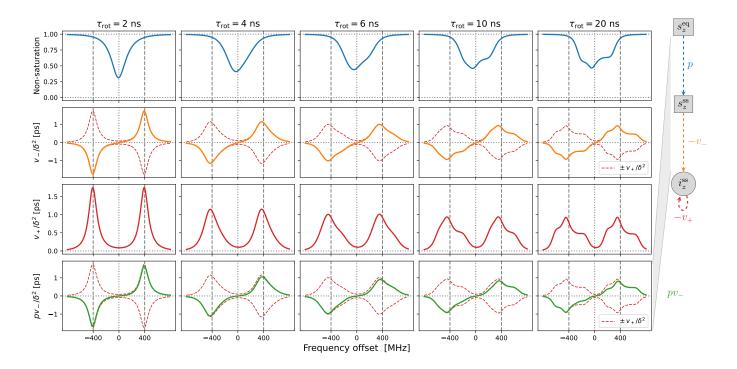
Figure 3. Solid-effect rates v_+ (red line) and pv_- (green line) calculated at high mw power ($B_1 = 5.5$ G) for static dipolar interaction (i.e., 'solid') and several different rates of rotational tumbling. The factorization of pv_- into p (blue line) and v_- (orange line) is also shown. All other parameters as in fig. 2 and $L_{\max} = 10$. In particular, $T_1 = 100$ ns.

SE. We show p and v_-/δ^2 in the first two rows of fig. 3. Note that v_+/δ^2 and pv_-/δ^2 were calculated directly from (92), whereas v_-/δ^2 was determined by dividing pv_-/δ^2 by $p = 1 - \omega_1^2 T_1 [\mathbf{P}_0^{-1}]_{11}$ (eq. (75)).

The columns in fig. 3 reveal the effect of the g-tensor anisotropy on the different factors relevant to SE. v_+/δ^2 in the third row of the figure is composed of two SE lines centered at $-\omega_I$ and $+\omega_I$. At the fastest tumbling (leftmost column), each of these two lines is symmetric and approximately Lorentzian. When the tumbling slows down, each line broadens and becomes asymmetric. At the slowest tumbling rate (rightmost column), each line resembles a powder EPR spectrum with anisotropic g tensor. We see that in the regime of slow tumbling the profile of v_+/δ^2 is no longer symmetric (i.e., even) with respect to the electronic resonance at zero offset frequency.

In the second row of fig. 3 we show v_-/δ^2 (orange line), which is also composed of two SE lines centered at $-\omega_I$ and $+\omega_I$, with the former flipped with respect to the horizontal axis. For comparison, in the second row we also plotted v_+/δ^2 and $-v_+/\delta^2$ (dashed red lines). We see that, for all tumbling rates, the two SE lines comprising v_-/δ^2 exactly match their counterparts in v_+/δ^2.

The first row of fig. 3 shows the electronic saturation under g-tensor anisotropy (we actually plot the "non-saturation" $p = 1 - s$). Because of the large B_1 used in the calculations ($B_1 = 5.5$ G) appreciable electronic saturation is achieved for

520 all shown tumbling rates. From the perspective of the solid effect, it is noteworthy that the saturation is more localized to on-resonance conditions when the g-tensor anisotropy is averaged out by the tumbling, and spreads to larger off-resonance frequencies when the tumbling slows down. This spread broadens the saturation profile and reduces its maximum. However, in spite of the substantial increase of the spectral width of the saturation when going from $\tau_{\mathrm{rot}} = 2\,\mathrm{ns}$ to $\tau_{\mathrm{rot}} = 20\,\mathrm{ns}$, the maximum decreases only moderately, remaining close to 50% at the slower tumbling rate.

525 Of course, the amplitude of the saturation profile depends not only on B_1 but also on the electronic T_1 relaxation time. To illustrate this dependence, we recalculated all curves in fig. 3 after increasing T_1 five-fold to 500 ns. The result, which is shown in fig. A1, demonstrates larger saturation for all tumbling rates. At the same time, v_-/δ^2 and v_+/δ^2 (second and third rows) remain entirely unaffected. This demonstrates that the SE lines do not experience the power-broadening that affects the EPR spectrum.

530 Finally, the last row of fig. 3 shows pv_-/δ^2 (solid green line), which equals the product of the first and second rows. From (7) we know that pv_-/δ^2 basically gives the SE-DNP spectrum, up to an overall scaling factor. Since pv_- is suppressed by the electronic saturation compared to v_-, we see that pv_-/δ^2 is somewhat reduced at offsets between the canonical SE positions $\pm\omega_I$. Because both the electronic saturation profile and the profile of v_- are asymmetric in the slow motional regime where the EPR line exhibits clear g-broadening, the line shape of the SE-DNP spectrum (proportional to pv_-) is no longer antisymmetric

535 (i.e., odd) with respect to the electronic resonance. This is most visible for the green line in the lower rightmost corner of fig. 3.

4.5 Solid effect in liquids

In the light of Sec. 3.3, the generalization to liquids consists of calculating the matrix

$$\mathcal{Q} = j_{11}(\mathcal{B}), \tag{93}$$

540 and using it instead of $\mathcal{B}^{-1}$ in (87):

$$R_{1I}^A = \langle\delta^2\rangle\mathrm{Re}\{[[\mathcal{Q}_{\omega_1=0}]_{zz}]_{11}\}$$
$$v_+ = \langle\delta^2\rangle\mathrm{Re}\{[[\mathcal{Q}]_{zz}]_{11}\} - R_{1I}^A$$
$$pv_- = -\langle\delta^2\rangle\omega_1\mathrm{Im}\{[([\mathcal{Q}]_{zx} + [\mathcal{Q}]_{zy}\mathbf{R}_2^{-1}\boldsymbol{\Delta})\mathbf{P}_0^{-1}]_{11}\}. \tag{94}$$

Because the zz sub-block of $\mathcal{B}$ is diagonal and does not couple to the rest when $\omega_1 = 0$, we deduce that

$$R_{1I}^A = \langle\delta^2\rangle\mathrm{Re}\{j_{11}(R_1 + \mathrm{i}\omega_I)\}, \tag{95}$$

which is identical to (43). Thus, as we already observed for 'solids', the expression for R_{1I}^A is not affected by the anisotropy of

545 the g tensor and the slow tumbling of the radical.

In fig. 4 we show the same properties as in fig. 3 but now in the presence of translational diffusion treated by the FFHS model with motional time scale $\tau_{\mathrm{ffhs}} = 6\,\mathrm{ns}$. Several changes compared to 'solids' (fig. 3) are worth pointing out.
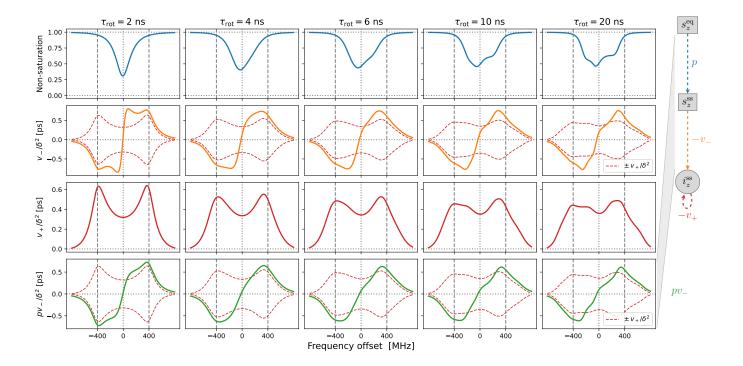
Figure 4. Same as fig. 3 for the FFHS model of translational diffusion with $\tau_{\mathrm{ffhs}} = 6\,\mathrm{ns}$.

In line with our previous understanding (Sezer, 2023b), the SE lines comprising $v_+/\langle\delta^2\rangle$ are broadened by the translational motion that modulates the dipolar interaction (red lines in the third row of fig. 4). This motional broadening reduces their maximum intensities compared to 'solids' (fig. 3, third row). Previously, in the case of Lorentzian lines, the reduction of intensity in the transition from solids to liquids was dramatic, by more than a factor of ten (Sezer, 2023b, figs. 3, 4 and 5). In contrast, the reduction in the presence of g-tensor broadening is about a factor of two (compare third rows of figs. 3 and 4). This observation may help rationalize why the maximum SE-DNP enhancement in liquids, e.g., about 50 for trityl in glycerol at 320 K (Kuzhelev et al., 2023), is not negligibly smaller compared to the enhancements that are obtained in the solid state. We also point out that, while reducing the maximum SE intensities in the vicinity of $\pm\omega_I$, the motional broadening substantially increases the intensities at the smaller offsets around the electronic resonance.

Besides the motional broadening, the progression from left to right in the third row of fig. 4 demonstrates additional g-tensor broadening, which was present also in 'solids'. However, now the two SE lines are affected differently by the g-tensor anisotropy, making the profile of $v_+/\langle\delta^2\rangle$ at slow tumbling rates rather irregular.

Moving on to the second row in fig. 4, we see that the SE lines that make up $v_-/\langle\delta^2\rangle$ (orange) are now completely different from their counterparts in $v_+/\langle\delta^2\rangle$ (dashed red). The increased intensity in the vicinity of the electronic resonance due to motional broadening is also manifested by $v_-/\langle\delta^2\rangle$. For the fastest tumbling in the figure (leftmost column), the fluctuations of the dipolar interaction not only broaden the SE lines but also enable a new phenomenon, which is manifested as near-resonance

peaks that are comparable in magnitude to the peaks at $\pm\omega_I$ but clearly distinct from them (orange line). These peaks reflect
the multiplicative contribution of the dispersive EPR signal to v_- (Sezer, 2023a, b). For faster translational diffusion the near-
resonance peaks may become larger than the peaks at $\pm\omega_I$, as can be seen in the leftmost column of fig. A3a (orange line).
Because they are more strongly suppressed by the electronic saturation, however, these peaks do not exceed the SE peaks in
the final enhancement profile (fig. A3a, leftmost column, green line).

Up to an overall scaling factor, the green lines in the last row of fig. 4 correspond to the SE-DNP enhancement profile.
Because its middle part is suppressed by the electronic saturation, this profile in the presence of g-tensor broadening becomes
very non-symmetric and responds sensitively to the tumbling of the polarizing agent. To further illustrate the influence of
the electronic saturation on the SE-DNP spectrum, in fig. A2 we show the same curves but calculated with five-fold longer
electronic spin-lattice relaxation time ($T_1 = 500$ ns), which leads to larger saturation. Similarly, to illustrate the effect of trans-
lational diffusion, we recalculated the curves in fig. 4 for $\tau_{\rm ffhs} = 3$ ns (two times faster) and $\tau_{\rm ffhs} = 12$ ns (two times slower).
The results are presented in fig. A3. These additional simulations show that the SE-DNP line shape is very sensitive to the
times scales of molecular motion.

In the next section, we systematically vary the degrees of power broadening and motional broadening to match the experi-
mental DNP profiles from fig. 1.

5   Disentangling the solid and Overhauser DNP effects

Using the developed methodology, we now analyze the experiments from fig. 1. In the light of eqs. (2) and (7) for the OE
and SE enhancements, we will identify the profile of the electronic saturation (fig. 4, first row) with $\epsilon_{\rm OE}$ and the profile of
$pv_-/\langle\delta^2\rangle$ (fig. 4, last row, green line) with $\epsilon_{\rm SE}$. The tumbling times to be used in the DNP calculations will be obtained by
fitting the experimental cw-EPR spectra. We start with 10-Doxyl-PC (fig. 1a,c) as its experimental spectra were more amenable
to unrestricted fits of all parameters.

5.1   10-Doxyl-PC

5.1.1   Fit to the cw-EPR spectrum

Derivative EPR spectra were calculated from the first (i.e., 00th) components of the expressions in (77) for different values
of the fitting parameters. In the fit, we varied the time scale of tumbling, $\tau_{\rm rot}$, as well as the g-tensor anisotropies γ_0^2 and γ_2^2
(eq. (50)). As we have no precise knowledge of the field B_0 at the sample, we freely shifted the calculated spectra along the
horizontal axis to achieve best match with experiment. Since this leaves one of the g-tensor components undetermined we took
$g_{zz} = 2.0023$, which is typical for nitroxides.

The numerical integrals of the derivative EPR spectra in figs. 1a and 1b (dotted-dashed blue lines) do not come down exactly
to zero at the end of the integration range at high frequency offsets. This points to the possibility that the in-phase component,
s_y, is mixed slightly with the out-of-phase component, s_x. To account for this possibility, we fitted the derivative EPR spectra

595   by calculating

$$\frac{\partial s_y^{00}}{\partial \Delta} \cos \phi + \frac{\partial s_x^{00}}{\partial \Delta} \sin \phi, \tag{96}$$

where the angle ϕ controlled the degree of mixing.

All in all, not counting the shift along the horizontal axis, we had four fitting parameters: γ_0^2, γ_2^2, $\tau_{\rm rot}$ and ϕ. The best fit to the cw-EPR spectrum of 10-Doxyl-PC is shown in fig. 5a. The corresponding fitting parameters are given in the upper half of

600   Table 1.

Encouragingly, our fitted spectrum shows rather good agreement with experiment, in spite of the simplifying assumptions of the theoretical model, namely isotropic rotational diffusion and absence of hyperfine interaction. To check the effect of the latter on the cw-EPR spectrum, we used Easyspin (Stoll and Schweiger, 2006) to simulate spectra with our fitted parameters but now also including a nitroxide hyperfine tensor, $A = \mathrm{diag}(14, 14, 90)\,\mathrm{MHz}$. The result is given in fig. A4a. The modification due to

605   the hyperfine interaction, although small as expected at high magnetic fields, is clearly visible. Nevertheless, the comparison of the integrals of the cw-EPR spectra in fig. A4b suggests that the error made by neglecting the hyperfine interaction when calculating the DNP spectrum should be small.

Regarding the values of the fitted parameters, it was encouraging to see that the fit resulted in a negligibly small mixing angle of $\phi = -1.3°$, indicating that the measured spectrum correctly reflects the in-phase EPR component. With $B_0 = 9.4029\,\mathrm{T}$ and

610    $g_{zz} = 2.0023$, the fitted g-tensor anisotropies that are given in Table 1 implied

$$g_{xx} = 2.00755, \qquad g_{zz} = 2.00555. \tag{97}$$

These values are rather reasonable for a nitroxide spin label. Finally, the fitted time scale of rotational diffusion was $\tau_{\rm rot} = 5.2\,\mathrm{ns}$. For comparison, the same time scale for the nitroxide free radical TEMPOL in water is about $20\,\mathrm{ps}$ (Sezer et al., 2009). However, unlike TEMPOL, our spin label is covalently attached to the lipid chain.

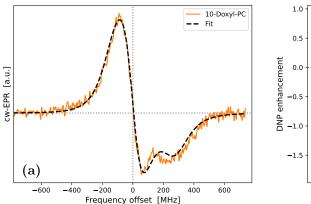615   **5.1.2   Fit to the DNP spectrum**

Fixing the g-tensor components and the tumbling time to the values obtained from the fit to the cw-EPR spectrum, we proceeded to fit the DNP spectrum of 10-Doxyl-PC (fig. 1c). In the calculations, we fixed the mw field to $B_1 = 5.5\,\mathrm{G}$, which is our best estimate for the home-built Fabry-Pérot resonator operating at maximum power (Denysenkov et al., 2022). During the fits, we again allowed for global shift of the calculation along the horizontal axis. In addition, we fitted the electronic T_1 time,

620   which has a direct effect on the electronic saturation profile, as well as the time scale of translational diffusion, $\tau_{\rm ffhs}$, which is responsible for the motional broadening of the SE lines.
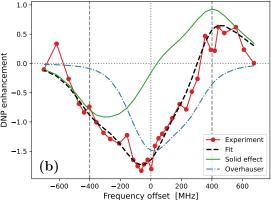
In the fit, we calculated the electronic saturation factor (eq. (75)) and the time scale $pv_-(\Delta)/\langle \delta^2 \rangle$ (last equation in (94)) as functions of the offset frequency Δ. Up to unknown multiplicative factors, these correspond to, respectively, the OE and SE enhancement profiles (eqs. (2) and (7)). We then fit the experimental DNP spectrum by calculating

625    $$\epsilon(\Delta) = \sigma_{\rm OE} \times s(\Delta) + \sigma_{\rm SE} \times \frac{pv_-}{\langle \delta^2 \rangle}(\Delta), \tag{98}$$

Figure 5. Fits to the experimental cw-EPR spectrum (**a**) and DNP spectrum (**b**) of 10-Doxyl-PC. In both cases, our best fits are shown with dashed black lines. The DNP spectrum in (**b**) is calculated by adding the contributions of SE (solid green line) and OE (dotted-dashed blue line), both of which are affected by the g-tensor anisotropy. The fit parameters are given in Table 1.

Table 1. Parameters obtained from the fits to the experimental data. $B_1 = 0.02\,\mathrm{G}$ for EPR and 5.5 G for DNP. Homogeneous $T_2^{\mathrm{homog}} = 20\,\mathrm{ns}$ was used for both EPR and DNP.

fit	parameter	10-Doxyl-PC	16-Doxyl-PC	
EPR	γ_0^2, γ_2^2 (MHz)	$-373, 107$	from 10-PC	
	τ_{rot} (ns)	5.2	1.9	
	ϕ (°)	-1.3	-2	
	shown in figure	5a	6a	
DNP	τ_{ffhs} (ns)	6.4	from 10-PC	15.3
	T_1 (ns)	123	153	141
	σ_{OE} (-)	2.43	2.385	2.57
	σ_{SE} (ps^{-1})	1.51	1.35	1.09
	shown in figure	5b	6b	7

where the scaling parameters σ_{OE} and σ_{SE} were also allowed to vary freely. As a result, not counting the shift along the horizontal axis, our fit contained four fitting parameters: τ_{ffhs}, T_1, σ_{OE} and σ_{SE}. The best fit to the DNP spectrum of 10-Doxyl-PC is shown in fig. 5b. It is noteworthy how the total DNP enhancement (dashed black line) emerges from the sum of the SE (green line) and OE (dotted-dashed blue line) contributions. The corresponding fitting parameters are given in the bottom half 630 of Table 1.

In the case of 10-Doxyl-PC, the intuitive analysis of Neudert et al. (2017) for identifying the OE and SE components of a mixed DNP spectrum using the integrated cw-EPR line shape already performed very well (fig. 1c). It is, therefore, not surprising that our analysis, which has more fitting parameters, agrees better with the experimental DNP spectrum (fig. 5b).

Both deficiencies of the intuitive approach, namely, too narrow OE and SE contributions due to the lack of, respectively, power broadening and motional broadening, appear to be satisfactorily addressed.

On a more fundamental level, our simulation shows that, due to the simultaneous power- and motional-broadening, the OE and SE contributions to the DNP enhancement are not only rather asymmetric but also overlap extensively. It should, therefore, be practically impossible to extract any molecular information from the mixed DNP spectrum without a complex, quantitative analysis. In our specific case, the fit resulted in a translational time scale $\tau_{\mathrm{ffhs}} = 6.4\,\mathrm{ns}$, and suggested that the electronic relaxation time should be about $T_1 = 120\,\mathrm{ns}$. At the high magnetic field of the experiment ($B_0 = 9.4\,\mathrm{T}$) this spin-lattice relaxation time is practically impossible to measure in the liquid state.

In addition to τ_{ffhs} and T_1, the fit to the DNP spectrum of 10-Doxyl-PC also produced the following numerical values for the two scaling parameters in eq. (98): $\sigma_{\mathrm{OE}} = 2.4$ and $\sigma_{\mathrm{SE}} = 1.5\,\mathrm{ps}^{-1}$. These will be analyzed in Sec. 5.3 together with the corresponding values for 16-Doxyl-PC.

5.2 16-Doxyl-PC

Because the g-tensor anisotropies are largely averaged in the cw-EPR spectrum of 16-Doxyl-PC (fig. 1b), we did not attempt to fit them. Instead, we fixed all three components to the values obtained from 10-Doxyl-PC. This left only the rotational time, τ_{rot}, and the mixing angle, ϕ, as fitting parameters, not counting the shift along the horizontal axis. As the automated fitting did not behave well, we varied these two parameters manually. One satisfactory fit, obtained with the parameters that are given in Table 1, is shown in fig. 6a. We mention that the relative heights of the two lines in the calculation were slightly improved by using a small mixing angle of $\phi = -2°$.

Although, overall, the fit is not bad, the middle part of the calculated spectrum changes too sharply and its high-frequency line is too narrow compared to experiment. We again used Easyspin to check whether these deficiencies are due to the lack of hyperfine interaction. The spectra for $\tau_{\mathrm{rot}} = 1.9\,\mathrm{ns}$ with and without hyperfine interaction are shown in fig. A5a. As the whole spectrum is narrower than that of 10-Doxyl-PC, the effect of the hyperfine tensor is comparatively larger. Nonetheless, the integrated EPR lines in fig. A5b show that the extra width due to the hyperfine tensor should not compromise our subsequent analysis of the DNP spectrum, which will experience additional power-broadening and motional-broadening.

Moving on to the DNP spectrum, we observed that the free fit of all parameters resulted in τ_{ffhs} that was more than two times larger than that of 10-Doxyl-PC, as we explain below. Considering this to be unrealistic, we fixed τ_{ffhs} to the value that was obtained from 10-Doxyl-PC. Thus, not counting the horizontal translation of the calculated DNP spectrum, our automated fit had three fitting parameters: T_1, σ_{OE} and σ_{SE}. The outcome is shown in fig. 6b. The corresponding parameters are given in the second-last column of the lower half of Table 1.

At 9.4 T the electronic Larmor precession time scale is about half a picosecond, which is three orders of magnitude less than the rotational time scales inferred from the cw-EPR spectra. On such sub-ps time scales, the local dynamics of the spin labels at positions 10 and 16 should not be very different from each other. Since the spin-lattice relaxation is determined by dynamics on the electronic Larmor time scale, we were satisfied that the fitted $T_1 = 150\,\mathrm{ns}$ was close to that from 10-Doxyl-PC.
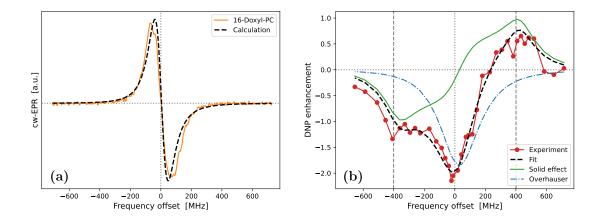
Figure 6. Same as fig. 5 but for 16-Doxyl-PC. The fitted parameters are given in the second to last column of Table 1. Because all fitted lines in figs. 5, 6 and 7 are calculated only at the experimental offsets, the green SE lines are not perfectly smooth.

The performance of the simple analysis of Neudert et al. (2017) was poorer for 16-Doxyl-PC (fig. 1d). Compared to it, our fit to the DNP enhancement profile is excellent (fig. 6b). The only part of the DNP spectrum that our calculation systematically underestimates are the five leftmost experimental points. Although there are other individual experimental points that lie further from the calculated spectrum, these five points are persistently lower by about 0.2 enhancement units.

Observe that the downward shift of the fifth experimental point (together with the first four points) produces an enhancement peak at around $-400\,\mathrm{MHz}$. The only way our automated fit can create a pronounced peak at this offset is by making the SE contribution (green line) more "solid-like", i.e., by increasing τ_{ffhs} and reducing the motional broadening. (The lower left corner of fig. A3b provides an example of such more solid-like SE line shape.) We thus identify the systematic displacement of the leftmost five points to be responsible for the increase of τ_{ffhs} when it is allowed to vary freely during the fit.

The best fit that we obtained when τ_{ffhs} was included among the other fitting parameters is shown in fig. 7. (The resulting fit parameters are given in the last column of the lower half of Table 1.) Indeed, with $\tau_{\mathrm{ffhs}} = 15.3\,\mathrm{ns}$, the SE lines (green) have become sharper and a small enhancement peak at $-400\,\mathrm{MHz}$ has emerged (dashed black line). Although the enhancement around $+400\,\mathrm{MHz}$ has been compromised in the process, the overall fit to all experimental points is improved compared to fig. 6b.

The two alternative fits in figs. 6b and 7 correspond to very different time scales of translational diffusion. Nevertheless, within the variability of the measurements, they both agree with the DNP data. Considering the experimental challenges of liquid-state DNP at such high magnetic fields and large mw powers, further decreasing the experimental variability will be very hard. It is, therefore, important to analyze together several different experimental constructs, like our 10- and 16-Doxyl-PC. The final decision of which fit to the DNP spectrum of 16-Doxyl-PC is "better" can only be based on the overall consistency of the fitted parameters across all analyzed data. We return to this point in Sec. 5.3.
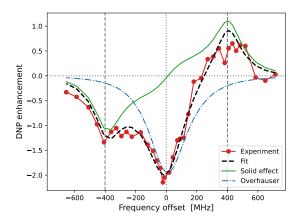
Figure 7. Same as fig. 6b but also fitting τ_{ffhs}. The fitted parameters are given in the last column of Table 1. Observe that the OE contribution to the DNP spectrum (dotted-dashed blue line) is narrower (i.e., more "liquid-like") than that of 10-Doxyl-PC (fig. 5b), while the SE contribution is more "solid-like" because the time scale τ_{ffhs} is 2.4 times longer.

The other two parameters that emerged from the fit to the DNP spectrum of 16-Doxyl-PC were σ_{SE} and σ_{OE}. These determine the amplitudes of the SE contribution (solid green lines in figs. 6b and 7) and OE contribution (dotted-dashed blue lines) to the DNP enhancement (dashed black lines). We now turn to the analysis of these scaling parameters.

5.3 Additional molecular parameters

Ultimately, the motivation to disentangle a mixed DNP spectrum into its OE and SE components lies in the desire to extract information about the molecular and spin properties that the respective DNP mechanism depends on. The main advantage of our procedure over the intuitive approach of Neudert et al. (2017) is that our decomposition produces physically interpretable parameters, like τ_{ffhs} and T_1. In addition, our scaling parameters σ_{OE} and σ_{SE} multiply, respectively, the saturation factor and $v_-/\langle\delta^2\rangle$, whose absolute magnitudes are part of the calculation (fig. 4, vertical axes). Thus, we can extract further information from the fitted values of σ_{OE} and σ_{SE}. In contrast, because the simple approach rescales the integrated cw-EPR spectrum whose amplitude is arbitrary, the values of its scaling factors are not informative.

Using eq. (2) for the OE enhancement, the coupling factor c is readily expressed in terms of σ_{OE}:

$$c = \frac{\sigma_{\text{OE}}}{f} \frac{\gamma_I}{|\gamma_S|}, \tag{99}$$

where the leakage factor f can be obtained by measuring the nuclear spin-lattice relaxation times (eq. (4)).

We measured the T_1 values for the chain protons of DOPC (without spin-labeled lipids) at 310 K and 330 K using the Fabry-Pérot probe. These are given in the T_{1I}^0 column of Table 2. Additionally, we measured the nuclear spin-lattice relaxation times in the presence of either 10- or 16-Doxyl-PC (column T_{1I} of Table 2). The target temperature of the DNP experiments (320 K) lies between the two temperatures at which the nuclear T_1 times were measured. However, considering the possibility of mild

Table 2. Analysis of the scaling parameters $\sigma_{\rm OE}$ and $\sigma_{\rm SE}$. Nuclear spin-lattice relaxation times with (T_{1I}) and without (T_{1I}^0) spin labels were measured at two different temperatures. These determine the leakage factor f. The coupling factor c is obtained from f and $\sigma_{\rm OE}$ using eq. (99). The magnitude of the dipolar interaction responsible for SE ($\langle\delta^2\rangle$), obtained from $\sigma_{\rm SE}$ using eq. (100), provides information about the effective contact distance (b). Combining b with $\tau_{\rm ffhs}$ from Table 1, we estimate the diffusion constant of the FFHS model ($D_{\rm ffhs}$).

| | Temp. | Nuclear T_1's | | Overhauser | | | Solid effect | | | |
Doxyl-PC	T (K)	T_{1I}^0 (ms)	T_{1I} (ms)	f	$\sigma_{\rm OE}$	c (‰)	$\sigma_{\rm SE}$ (ps^{-1})	$\langle\delta^2\rangle T_{1I}$ (ns^{-1})	b (nm)	$D_{\rm ffhs}$ (nm^2/μs)
10	310	580	44	0.92	2.43	3.99	1.51	2.29	0.61	59
	330	910	52	0.94		3.92			0.65	66
16	310	580	93	0.84	2.385	4.32	1.35	2.05	0.81	104
	330	910	120	0.87		4.17			0.89	123
16*	310	"	"	"	2.57	4.65	1.09	1.66	0.87	50
	330	"	"	"		4.50			0.95	59

705 temperature rise by several degrees, we expect the values at 330 K to closely reflect the DNP conditions. Nonetheless, we carry out the following analysis using the T_1 values measured at both 310 K and 330 K.

The leakage factors obtained from (4) are shown in the column f of Table 2. Using the values of $\sigma_{\rm OE}$ from Table 1 in (99), we arrived at the coupling factors in column c of Table 2. In the case of 16-Doxyl-PC, the analysis was performed for the fit where $\tau_{\rm ffhs}$ was fixed at 6.4 ns (denoted 16 in Table 2) as well as for the fit where $\tau_{\rm ffhs}$ was free to change (denoted 16*).

710 (These two alternatives correspond to the last two columns of Table 1.) For both choices, somewhat larger coupling factors were deduced for 16-Doxyl-PC compared to 10-Doxyl-PC. The estimated coupling factors are less than two times smaller than what we have obtained previously for TEMPOL in DMSO, and about four times smaller than the coupling factors between TEMPOL and the protons of toluene (Prisner et al., 2016; Sezer, 2013; Küçük et al., 2015).

Turning now to SE, using the enhancement in (7) we express the unknown strength of the dipolar interaction in terms of the

715 scaling parameter $\sigma_{\rm SE}$ as follows:

$$\langle\delta^2\rangle T_{1I} = \sigma_{\rm SE}\frac{\gamma_I}{|\gamma_S|}. \tag{100}$$

The values of $\langle\delta^2\rangle T_{1I}$, which were calculated from the right-hand side of (100), are about $2\,{\rm ns}^{-1}$ for 10, 16 and 16* (Table 2). Since $v_+/\langle\delta^2\rangle$ is about 1 ps (fig. 4, third row), we conclude that $v_+ T_{1I} \ll 1$, which justifies our use of the approximation (7) throughout the analysis, including during the fit to the DNP spectra.

720 From the expression of $\langle\delta^2\rangle$ (eq. (39)), we can write the contact distance of the translational FFHS model as

$$b^3 = N\frac{2\pi}{5}D_{\rm dip}^2\frac{T_{1I}}{\sigma_{\rm SE}}\frac{|\gamma_S|}{\gamma_I}, \tag{101}$$

where N is the number density of the electronic spins. Since, in principle, all parameters on the right-hand side of (101) are measurable, we can determine b. To estimate N, we note that the molecular volume of DOPC is $1.3\,{\rm nm}^3$ (Greenwood et al., 2006). Since there are 20 unlabeled lipids for one labeled one, we estimate $N = (20 \times 1.3\,{\rm nm}^3)^{-1}$, which corresponds to a

725   molar concentration of 64 mM. Using this number in (101), we obtained the values of b that are given in the second to last
column of Table 2.

When the values of b are interpreted literally as "contact distance" between the nitroxide spin label and the protons of the
lipid chains, their substantial variation between 10- and 16-Doxyl-PC is disturbing. From that perspective, it is clear that the
parameter b of the FFHS model, which we used to account for the fluctuations of the dipolar interaction due to molecular
730   translations, cannot reflect the actual molecular distances of closest approach.

Because b was obtained from the scaling parameter σ_{SE}, only information about the *amplitude* of the SE enhancement has
been directly used in its estimate. In contrast, the motional time scale τ_{ffhs} (Table 1) encodes information about the *line shape*
of the SE enhancement. From these complementary features of the SE contribution to the DNP spectrum, we have managed to
determine both b and τ_{ffhs}. Having access to these two parameters, we can calculate the diffusion constant of the FFHS model
735   from (38). The results are given in the last column of Table 2. To our surprise, we obtained very similar values for 10 and 16*,
while the diffusion constant for 16 is two-fold larger. (Given the variability in the experimental data and the fact that the fits to
the DNP spectra are not unique, the differences between D_{ffhs} of 10 and 16* should not be seen as meaningful.)

In an effort to identify a potential candidate for the physical motion that the FFHS model emulates, we observed that the
coefficients of lateral translational diffusion for DOPC in oriented bilayers are $20\,\mathrm{nm}^2\,\mu\mathrm{s}^{-1}$ at 323 K, and $26\,\mathrm{nm}^2\,\mu\mathrm{s}^{-1}$ at 333 K
740   (Filippov et al., 2003, fig. 6a). These, we expect, bracket the value at our DNP conditions. The diffusion in the FFHS model
corresponds to the *relative* translation of the nuclear and electronic spins, i.e., $D_{ffhs} = D_I + D_S$. Assuming that the lateral
diffusion of spin-labeled PSPC in a DOPC bilayer is similar to that of DOPC, from the measured values given above we would
expect D_{ffhs} between 40 and $52\,\mathrm{nm}^2\,\mu\mathrm{s}^{-1}$. This range is surprisingly close to the estimates of 10 and 16* in the last column of
Table 2, which suggests that the FFHS model in our analysis likely accounts for the lateral diffusion of the lipids in the plane
745   of the bilayer.

Since it leads to a diffusion constant that is similar to (i) the known lateral diffusion of DOPC and (ii) the estimate obtained
for 10-Doxyl-PC, we conclude that the fit to the DNP spectrum of 16-Doxyl-PC that is shown in fig. 7 (i.e., the one that led
to "unreasonably" large τ_{ffhs}) is more realistic than the one with fixed τ_{ffhs} (fig. 6b). From the perspective of the diffusion
constant, the longer motional time scale of 16* compared to 10, which resulted in more solid-like SE line shape with less
750   motional broadening, reflects the fact that the "contact distances" in the two cases are different. In retrospect, it is amazing
how the independent estimates of b and τ_{ffhs} combine to yield practically identical diffusion constants for the two spin-labeling
positions.

At the moment, it is not clear to us how to properly interpret the different values of b at positions 10 and 16. Atomistic
molecular dynamics simulations (Oruç et al., 2016) could, in principle, be used to investigate whether these effective contact
755   distances reflect differences in proton density along the normal of the lipid bilayer, or arise for some other reason.

MAGNETIC
RESONANCE
Open Access
Discussions

6 Conclusion

In the time-domain description of SE that we developed recently (Sezer, 2023a), the relevant spin dynamics is pictured in terms of two connected Bloch equations. Due to this central role of the Bloch equations in our formalism, we first rephrased Freed's treatment of slow tumbling as a generalization of the classical Bloch equations, where the scalar elements of the Bloch matrix

760   became matrices in the space of the angular-momentum indices LM. For this reformulation to work, we had to neglect the hyperfine interaction, which is in fact treated by Freed et al. (1971). As a result, our analysis is formally deficient for nitroxide radicals. Nevertheless, it should be valid approximately at high magnetic fields where the influence of the hyperfine tensor is smaller than that of the g tensor. The experimental data that we analyzed fell into this regime.

DNP experiments with nitroxide free radicals in viscous liquids invariably manifest a mixture of SE and OE (Leblond et al.,

765   1971b; Neudert et al., 2017). As these two DNP mechanisms are sensitive to molecular motions on vastly different time scales, it should be possible to obtain rich dynamical information by analyzing their contributions to the overall DNP enhancement. Disentangling the SE and OE contributions, however, has proven to be challenging (Leblond et al., 1971a). Here we fitted liquid-state DNP spectra by calculating enhancements that were affected by both the translational diffusion of the spins and the rotational diffusion of the free radical. Since different motions modify the amplitude and the shape of the DNP spectrum in a

770   highly concerted manner, by fitting the entire line shape of the enhancement we also gained access to the absolute magnitudes of the SE and OE contributions.

Our current treatment of SE-DNP in liquids uses only the correlation function of the dipolar interaction to describe the translational motion of the spins (Sezer, 2023b). This is formally correct only when the diffusion is much faster than the nuclear T_1 relaxation. It should be possible to relax this condition and model slower spin diffusion, as relevant for SE in the

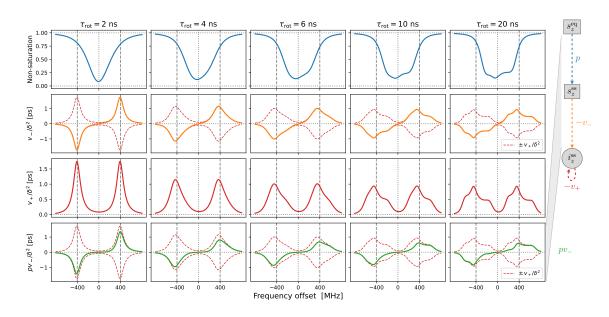775   solid state.

Appendix A: Additional figures

Figure A1. Same as fig. 3 but with $T_1 = 500$ ns (i.e., five-fold longer), which leads to larger saturation of the allowed electronic transition. Only the first and last rows are affected.
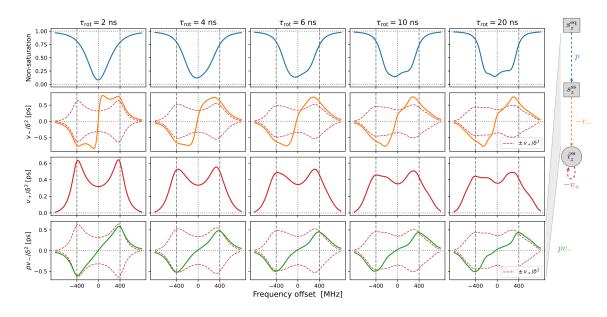

Figure A2. Same as fig. 4 but with $T_1 = 500$ ns, which leads to larger electronic saturation. As in the case of 'solids', only the first and last rows are affected.
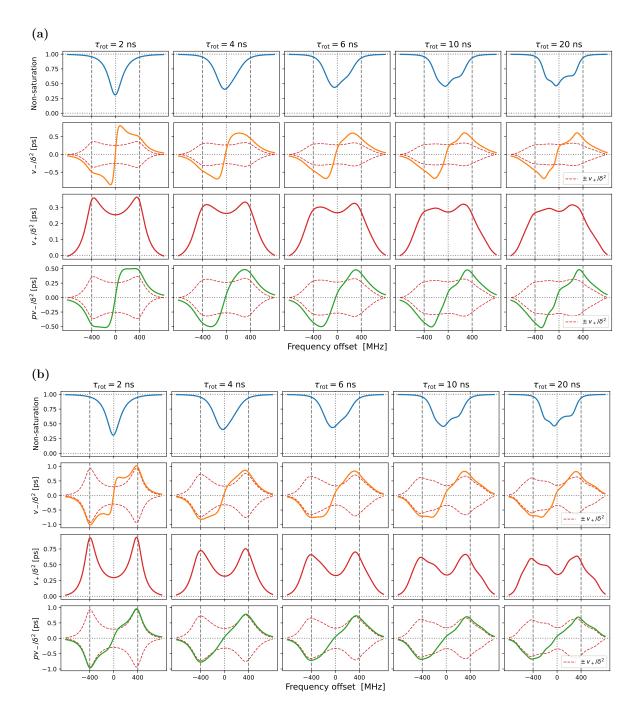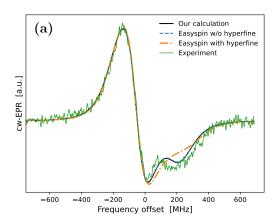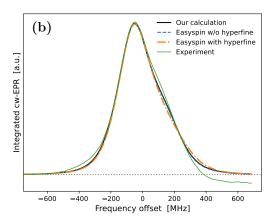
Figure A3. Same as fig. 4 but with (**a**) $\tau_{\text{ffhs}} = 3$ ns, i.e., two-fold faster translational motion which broadens the SE lines to a larger extent, and (**b**) $\tau_{\text{ffhs}} = 12$ ns, i.e., more solid-like behavior. Observe how the predicted SE-DNP line shape (green line in the last row) responds sensitively to the time scale of the translational motion that is responsible for averaging the dipolar interaction.
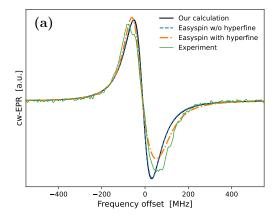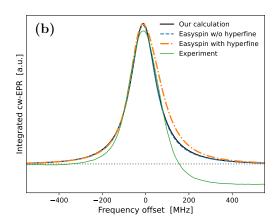
Figure A4. Effect of hyperfine tensor on the calculated EPR spectrum of 10-Doxyl-PC. Various derivative cw-EPR spectra (**a**) and their numerical integrals (**b**) are compared with each other. Our calculation (solid black line) agrees perfectly with the Easyspin (Stoll and Schweiger, 2006) simulation without a hyperfine tensor (dashed blue line). Including a hyperfine tensor with components $(14, 14, 90)$ MHz in the Easyspin calculation (dotted-dashed orange line) leads to visible changes in the derivative cw-EPR spectrum. However, the difference of the integrated EPR lines with and without a hyperfine tensor in (**b**) should be negligible as far as the simulation of the DNP spectrum is concerned.

Figure A5. Same as fig. A4 but for 16-Doxyl-PC. Because the cw-EPR spectrum is narrower to begin with, the relative contribution of the hyperfine tensor with components $(14, 14, 90)$ MHz is larger than in the case of 10-Doxyl-PC. Considering that the EPR line will experience additional power-broadening and motional-broadening in DNP, it should still be possible to safely neglect the extra width that the hyperfine tensor brings to the integrated EPR line in (**b**).

Author contributions. TFP envisioned the presented high-field DNP experiments in lipid bilayers and acquired funding for their execution. DD carried out these EPR and NMR experiments, deconvoluted the measured NMR signals to calculate the presented DNP spectra for the lipid chain protons, and performed the reported Easyspin simulations. DS conceived of the presented analysis of the experimental data, 780 developed the reported theoretical and numerical framework, analyzed the data, and wrote the manuscript with feedback from all coauthors.

Competing interests. TFP is an associate editor of Magnetic Resonance.

References

785   Abragam, A.: The Principles of Nuclear Magnetism, Oxford University Press, New York, 1961.

Abragam, A. and Goldman, M.: Principles of dynamic nuclear polarisation, Reports on Progress in Physics, 41, 395, https://doi.org/10.1088/0034-4885/41/3/002, 1978.

Abragam, A. and Proctor, W. G.: Une nouvelle méthode de polarisation dynamique des noyaux atomiques dans les solides, Compt. rend., 246, 2253–2256, 1958.

790   Anderson, P. W.: A Mathematical Model for the Narrowing of Spectral Lines by Exchange or Motion, Journal of the Physical Society of Japan, 9, 316–339, https://doi.org/10.1143/JPSJ.9.316, 1954.

Ayant, Y., Belorizky, E., Alizon, J., and Gallice, J.: Calcul des densités spectrales résultant d'un mouvement aléatoire de translation en relaxation par interaction dipolaire magnétique dans les liquides, J. Phys. (Paris), 36, 991–1004, 1975.

Carver, T. R. and Slichter, C. P.: Experimental Verification of the Overhauser Nuclear Polarization Effect, Physical Review, 102, 975–980,
795   https://doi.org/10.1103/PhysRev.102.975, 1956.

Denysenkov, V., Dai, D., and Prisner, T. F.: A triple resonance (e, 1H, 13C) probehead for liquid-state DNP experiments at 9.4 Tesla, Journal of Magnetic Resonance, 337, 107 185, https://doi.org/https://doi.org/10.1016/j.jmr.2022.107185, 2022.

Erb, E., Motchane, J.-L., and Uebersfeld, J.: Effet de polarisation nucléaire dans les liquides et les gaz adsorbés sur les charbons, Compt. rend., 246, 2121–2123, 1958a.

800   Erb, E., Motchane, J.-L., and Uebersfeld, J.: Sur une nouvelle méthode de polarisation nucléaire dans les fluides adsorbés sur les charbons. extension aux solides et en particulier aux substances organiques irradiées., Compt. rend., 246, 3050–3052, 1958b.

Filippov, A., Orädd, G., and Lindblom, G.: The Effect of Cholesterol on the Lateral Diffusion of Phospholipids in Oriented Bilayers, Biophysical Journal, 84, 3079–3086, https://doi.org/https://doi.org/10.1016/S0006-3495(03)70033-2, 2003.

Freed, J. H., Bruno, G. V., and Polnaszek, C. F.: Electron spin resonance line shapes and saturation in the slow motional region, The Journal
805   of Physical Chemistry, 75, 3385–3399, https://doi.org/10.1021/j100691a001, 1971.

Gizatullin, B., Mattea, C., and Stapf, S.: Field-cycling NMR and DNP –A friendship with benefits, Journal of Magnetic Resonance, 322, 106 851, https://doi.org/https://doi.org/10.1016/j.jmr.2020.106851, 2021a.

Gizatullin, B., Mattea, C., and Stapf, S.: Molecular Dynamics in Ionic Liquid/Radical Systems, The Journal of Physical Chemistry B, 125, 4850–4862, https://doi.org/10.1021/acs.jpcb.1c02118, 2021b.

810   Gizatullin, B., Mattea, C., and Stapf, S.: Three mechanisms of room temperature dynamic nuclear polarization occur simultaneously in an ionic liquid, Physical Chemistry Chemical Physics, 24, 27 004–27 008, https://doi.org/10.1039/D2CP03437A, 2022.

Greenwood, A. I., Tristram-Nagle, S., and Nagle, J. F.: Partial molecular volumes of lipids and cholesterol, Chemistry and Physics of Lipids, 143, 1–10, https://doi.org/https://doi.org/10.1016/j.chemphyslip.2006.04.002, 2006.

Hausser, K. H., Stehlik, D., and Waugh, J. S.: Dynamic Nuclear Polarization in Liquids, vol. 3, pp. 79–139, Academic Press,
815   https://doi.org/https://doi.org/10.1016/B978-1-4832-3116-7.50010-2, 1968.

Hwang, L.-P. and Freed, J. H.: Dynamic effects of pair correlation functions on spin relaxation by translational diffusion in liquids, J. Chem. Phys., 63, 4017–4025, 1975.

Kubo, R.: Note on the Stochastic Theory of Resonance Absorption, Journal of the Physical Society of Japan, 9, 935–944, https://doi.org/10.1143/JPSJ.9.935, 1954.

820   Kubo, R.: A Stochastic Theory of Line Shape, vol. XV, chap. 6, pp. 101–127, John Wiley & Sons. Inc., https://doi.org/https://doi.org/10.1002/9780470143605.ch6, 1969.

Küçük, S. E., Neugebauer, P., Prisner, T. F., and Sezer, D.: Molecular simulations for dynamic nuclear polarization in liquids: a case study of TEMPOL in acetone and DMSO, Physical Chemistry Chemical Physics, 17, 6618–6628, https://doi.org/10.1039/C4CP05832A, 2015.

Kuzhelev, A. A., Dai, D., Denysenkov, V., and Prisner, T. F.: Solid-like Dynamic Nuclear Polarization Observed in the Fluid Phase of Lipid
825   Bilayers at 9.4 T, Journal of the American Chemical Society, 144, 1164–1168, https://doi.org/10.1021/jacs.1c12837, 2022.

Kuzhelev, A. A., Denysenkov, V., Ahmad, I. M., Rogozhnikova, O. Y., Trukhin, D. V., Bagryanskaya, E. G., Tormyshev, V. M., Sigurdsson, S. T., and Prisner, T. F.: Solid-Effect Dynamic Nuclear Polarization in Viscous Liquids at 9.4 T Using Narrow-Line Polarizing Agents, Journal of the American Chemical Society, 145, 10 268–10 274, https://doi.org/10.1021/jacs.3c01358, 2023.

Leblond, J., Papon, P., and Korringa, J.: Stochastic Theory of Dynamic Spin Polarization in Viscous Liquids with Anisotropic Electron-Spin
830   Relaxation, Physical Review A, 4, 1539–1549, https://doi.org/10.1103/PhysRevA.4.1539, 1971a.

Leblond, J., Uebersfeld, J., and Korringa, J.: Study of the Liquid-State Dynamics by Means of Magnetic Resonance and Dynamic Polarization, Physical Review A, 4, 1532–1539, https://doi.org/10.1103/PhysRevA.4.1532, 1971b.

Müller-Warmuth, W., Meise-Gresch, K., and Waugh, J. S.: Molecular Motions and Interactions as Studied by Dynamic Nuclear Polarization (DNP) in Free Radical Solutions, vol. 11, pp. 1–45, Academic Press, https://doi.org/https://doi.org/10.1016/B978-0-12-025511-5.50007-4,
835   1983.

Neudert, O., Mattea, C., and Stapf, S.: A compact X-Band resonator for DNP-enhanced Fast-Field-Cycling NMR, Journal of Magnetic Resonance, 271, 7–14, https://doi.org/https://doi.org/10.1016/j.jmr.2016.08.002, 2016.

Neudert, O., Mattea, C., and Stapf, S.: Molecular dynamics-based selectivity for Fast-Field-Cycling relaxometry by Overhauser and solid effect dynamic nuclear polarization, Journal of Magnetic Resonance, 276, 113–121,
840   https://doi.org/https://doi.org/10.1016/j.jmr.2017.01.013, 2017.

Oruç, T., Küçük, S. E., and Sezer, D.: Lipid bilayer permeation of aliphatic amine and carboxylic acid drugs: rates of insertion, translocation and dissociation from MD simulations, Physical Chemistry Chemical Physics, 18, 24 511–24 525, https://doi.org/10.1039/C6CP05278A, 2016.

Papon, P., Motchane, J. L., and Korringa, J.: Unitary Theory of Dynamic Polarization of Nuclear Spins in Liquids and Solids, Physical
845   Review, 175, 641–649, https://doi.org/10.1103/PhysRev.175.641, 1968.

Prisner, T., Denysenkov, V., and Sezer, D.: Liquid state DNP at high magnetic fields: Instrumentation, experimental results and atomistic modelling by molecular dynamics simulations, Journal of Magnetic Resonance, 264, 68–77, https://doi.org/https://doi.org/10.1016/j.jmr.2015.11.004, 2016.

Redfield, A. G.: On the Theory of Relaxation Processes, IBM Journal of Research and Development, 1, 19–31,
850   https://doi.org/10.1147/rd.11.0019, 1957.

Sezer, D.: Computation of DNP coupling factors of a nitroxide radical in toluene: seamless combination of MD simulations and analytical calculations, Physical Chemistry Chemical Physics, 15, 526–540, https://doi.org/10.1039/C2CP42430D, 2013.

Sezer, D.: Non-perturbative treatment of the solid effect of dynamic nuclear polarization, Magn. Reson., 4, 129–152, https://doi.org/10.5194/mr-4-129-2023, 2023a.

855   Sezer, D.: The solid effect of dynamic nuclear polarization in liquids, Magn. Reson., 4, 153–174, https://doi.org/10.5194/mr-4-153-2023, 2023b.

Sezer, D., Gafurov, M., Prandolini, M. J., Denysenkov, V. P., and Prisner, T. F.: Dynamic nuclear polarization of water by a nitroxide radical: rigorous treatment of the electron spin saturation and comparison with experiments at 9.2 Tesla, Physical Chemistry Chemical Physics, 11, 6638–6653, https://doi.org/10.1039/B906719C, 2009.

860 Solomon, I.: Relaxation Processes in a System of Two Spins, Physical Review, 99, 559–565, https://doi.org/10.1103/PhysRev.99.559, 1955.

Stoll, S. and Schweiger, A.: EasySpin, a comprehensive software package for spectral simulation and analysis in EPR, Journal of Magnetic Resonance, 178, 42–55, https://doi.org/https://doi.org/10.1016/j.jmr.2005.08.013, 2006.

Wenckebach, T.: Essentials of Dynamic Nuclear Polarization, Spindrift Publications, The Netherlands, 2016.